RSC Applied Interfaces

ROYAL SOCIETY OF CHEMISTRY

REVIEW

View Article Online
View Journal | View Issue

Cite this: *RSC Appl. Interfaces*, 2026, 3, 293

Framework-stabilized metal nanostructures for next-generation photocatalysis

Bikash Chandra Dhal,†[a] Debadutta Samal,†[a] Debashis Acharya,[a] Subrat Swain,[a] Basudeb Dutta,[a] Srikanta Palei,[b] A. K. Tyagi,[c] Puspanjali Sahu*[d] and Rojalin Sahu*[a]

Received 24th November 2025,
Accepted 29th January 2026

DOI: 10.1039/d5lf00369e

rsc.li/RSCApplInter

Framework-stabilized metal nanostructures have emerged as a powerful class of catalysts, offering excellent activity, selectivity, and long-term stability. Encapsulation of nanoparticles (NPs) within porous crystalline frameworks such as metal–organic frameworks (MOFs) and covalent organic frameworks (COFs) effectively prevents aggregation, ensures accessibility of active sites, and enables efficient charge separation. This review provides a comprehensive analysis of synthesis protocols: *in situ*, post-synthetic, and one-pot methods, keeping in mind the crucial factors that dictate structural architectures. The role of reducing agents, solvents, functional groups, temperature, and framework nanoparticle interactions acts as the pivotal role in the structure–activity relationship. The stimulating role of such a catalyst system can be employed in the field of clean energy and sustainable development: hydrogen evolution reaction (HER), CO_2 reduction (CO_2RR), selective oxidation, and organic transformations are critically discussed to establish active materials in such applications. In particular, the challenges related to uniform encapsulation, framework stabilisation under reaction conditions, scalability, and recyclability are significantly accessed, together with future prospects in defect engineering, hybrid bimetallic systems, and enhanced light-harvesting abilities. Therefore, this review aims to provide an overview of catalysis, energy conversion, and materials science with a consolidated perspective on the fabrication of next-generation hierarchical frameworks.

1. Introduction

Nanostructures received significant attention from researchers owing to their catalytic efficiency.[1–5] However, owing to their high surface area, these structures exhibit thermodynamic instability and are prone to aggregation. The high surface energy of these nanostructures can be reduced by covering their surface with capping agents.[6,7] However, such surface coverings restrict surface accessibility and consequently reduce the catalytic efficiency of the nanostructures. Aggregation of nanostructures can also be prevented by confining them within supports such as zeolites and silica or making composites with graphene, MXene, *etc.*[8–10] However, this approach suffers from limitations such as uncontrolled growth of nanostructures and poor stability under harsh catalytic conditions.

Recently developed frameworks offer an efficient alternative to encapsulate nanostructures. These frameworks are an exclusive class of crystalline materials constructed through strong chemical bonds between organic molecules or organic molecules with metal ions.[2,11–18] Due to their captivating attributes, comprising varied chemical compositions, flexibility, large surface areas, and precisely defined pore architectures, frameworks have showcased significant potential as catalysts. Frameworks are predominantly used for various applications like storage and separation, carbon dioxide capture, drug delivery, sensing, and catalysis, marking them as a promising avenue for multilayered applications.[19–22] In particular, catalysts constructed by integrating nanoparticles within frameworks have garnered substantial interest within the catalysis community.[23–28] Encapsulation of NPs within frameworks blends the versatility of specially created organic matrices with the complexity of nanoscale engineering. This cooperative approach has paved the way for the development of catalysts that exhibit exceptional activity, stability and selectivity. The frameworks provide remarkable control over NP size, shape, and stability.

[a] *Future Materials Laboratory, Department of Chemistry, School of Applied Sciences, Kalinga Institute of Industrial Technology (KIIT) Deemed to be University, Bhubaneswar, Odisha, 751024, India. E-mail: rsahufch@kiit.ac.in*
[b] *Central Institute of Petrochemicals Engineering and Technology (CIPET): Institute of Petrochemicals Technology (IPT), B-25, CNI Complex, Patia, Bhubaneswar-751024, Odisha, India*
[c] *Homi Bhabha National Institute, Anushaktinagar, Mumbai, 400094, India*
[d] *Bhadrak (Autonomous) College, Bhadrak-756100, Odisha, India. E-mail: psahu.chem@gmail.com*
† These authors contributed equally to this work.

The overall theme of the metal nanoparticle-confined framework material is depicted in Scheme 1.

Further, these frameworks possess distinctive attributes that make them exceptionally well suited as hosts and substrates for NPs, resulting in a synergistic amplification of catalytic activity. Moreover, the existence of libraries of frameworks and NPs can provide a wide variety of catalysts suitable for a wide range of applications.[29,30] The past decade has seen notable advancements in the development of NP-encapsulated frameworks.[24,31–35] This review offers a comprehensive analysis of the variables influencing the development of these catalysts (NP-encapsulated frameworks). It also sheds light on the synergic influences of frameworks and NPs on the catalytic processes. Additionally, the current challenges associated with these encapsulated structures are discussed, as illustrated in Fig. 1.

Judicious analysis of Table 1 revealed a significant gap in correlating efficient catalytic activity with the role of framework-stabilized confinement effects. The synthesis and significant stability of metal clusters confined in frameworks remain challenging for broader aspects. Therefore, we aimed to establish strategies for nanostructure stabilization with reticular materials and to elucidate their role in photocatalysis.

Bikash Chandra Dhal

Bikash Chandra Dhal is a Ph.D. research scholar at the Kalinga Institute of Industrial Technology (KIIT) University, Bhubaneswar, India, under the supervision of Prof. Rojalin Sahu. He completed his B.Sc. from Angul Autonomous College, Angul, and his M.Sc. from Centurion University, Bhubaneswar. His research is devoted to the rational design and synthesis of metal–organic frameworks (MOFs) and MOF-derived functional architectures, with a strong emphasis on deciphering structure–property relationships. His work seeks to unravel framework chemistry, interfacial phenomena, and charge-transfer mechanisms to drive advancements in photocatalysis, electrochemical energy storage, and environmental remediation.

Debadutta Samal

Debadutta Samal is a Ph.D. Scholar in Chemistry working under the guidance of Prof. Rojalin Sahu in the School of Applied Sciences, KIIT Deemed to be University (KIIT DU), Bhubaneswar. Debadutta completed his M.Sc. in Chemistry from Ravenshaw University, Cuttack, and obtained his B.Sc. degree in Chemistry from BJB College, Bhubaneswar. His current research focuses on the design and development of metal–organic coordination compounds with particular emphasis on Schiff base compounds based on O/N donor ligands for potential applications. A significant part of his work involves the synthesis of metal helicates and the investigation of their biological applications.

Debashis Acharya

Debashis Acharya is pursuing a Ph.D. at the Kalinga Institute of Industrial Technology (KIIT) University, Bhubaneswar, India, under the supervision of Dr. Raghabendra Samantaray. His research focuses on understanding structure–function relationships in metal–organic frameworks (MOFs) and metal–oxo complexes, including ammonium peroxychromates. His work centers on elucidating the structural principles of coordination bonding and framework architectures. These inorganic systems are investigated for applications in heterogeneous catalysis and electrochemical processes, guided by structure–property correlations.

Subrat Swain

Subrat Swain is a Ph.D. researcher at the School of Applied Sciences, Kalinga Institute of Industrial Technology (KIIT) Deemed to be University, Bhubaneswar, India, working under the supervision of Prof. Rojalin Sahu. His research focuses on the design and synthesis of conducting polymer–metal–organic frameworks (MOFs) hybrid materials with enhanced electrical conductivity, optoelectronic properties, and environmental applications. So far, he has published thirteen original research articles in international journals, holds five Indian patents, and has contributed one book chapter. He has been a life member of the Society for Materials Chemistry (SMC-India), BARC, since 2023.

2. Encapsulation techniques for the nanostructures within frameworks

The well-designed structures of frameworks enable the effective encapsulation of a wide range of nanostructures. Methodologies developed so far can be divided into three broad categories. First, in the *in situ* synthesis method, metal ions are anchored on the skeleton of frameworks, and their successive reduction leads to the formation of nanostructures inside the pores of frameworks. Second, in a co-synthesis strategy, precursors of frameworks and nanoparticles can be mixed and used as starting materials to generate framework-encapsulated nanostructures. Finally, nanostructures can also be introduced into the pore of frameworks through post-synthetic modification. Together, these

Basudeb Dutta

Dr. Basudeb Dutta joined as an Assistant Professor at the Department of Chemistry, School of Applied Sciences, Kalinga Institute of Industrial Technology (KIIT) Deemed to be University, just after completing his Postdoctoral work under Nobel laureate Prof. Susumu Kitagawa at Kyoto University, Japan. Dr. Dutta's research focuses on the design and synthesis of coordination compounds, coordination polymers, and metal–organic frameworks (MOFs) and their applications in conductivity, catalysis, magnetism, sensing, Schottky diodes, crystal popping, and other areas. So far, he has published thirty-five original research articles (as first author) and eight review articles in the journals of international repute. He received the 'IUCr Young Scientist Award' in December 2019 at the 16th Conference of the Asian Crystallographic Association (AsCA 2019), National University of Singapore, Singapore.

Srikanta Palei

Dr. Srikanta Palei is currently working as an Assistant Professor at Central Institute of Petrochemical and Engineering Technology-IPT, Odisha, India. He obtained his PhD from Chonbuk National University and had more than 5 years of post-doctoral experiences from reputed institutes such as Ulsan National Institute of Science and Technology and Inha University, South Korea. He has more than 10 years of research experience in materials science research, specifically on solar cells, and more than two years of teaching experience. Numerous peer-reviewed journals have published his research.

A. K. Tyagi

Dr. A. K. Tyagi is currently Dean and Senior Professor at the Homi Bhabha National Institute, Mumbai, India. Other recent past positions include Director, Chemistry Group, Director, Bioscience Group, BARC, Mumbai, and Distinguished Scientist (DAE). He completed postdoctoral research at the Max-Planck Institute, Germany (1995–1996), and has since received numerous prestigious awards in recognition of his work. Dr. Tyagi's research interests cover areas of nanomaterials, functional materials, nuclear materials, metastable materials, and hybrid materials. During his scientific career spanning decades, he has published about 700 papers in international journals, 16 books, and several review articles and has to his credit 46 PhD students. He is also a Fellow of various national and international science and engineering academies and has been a visiting scientist at reputed institutions in six continents.

Puspanjali Sahu

Dr. Puspanjali Sahu is currently working as an Assistant Professor at Bhadrak Autonomous College, Odisha, India. She obtained her PhD from CSIR-National Chemical Laboratory and had more than 5 years of post-doctoral experience in reputed institutes such as Korea Advanced Institute of Science and Technology, South Korea; Indian Association for the Cultivation of Science, India, and CSIR-Institute of Minerals and Materials Technology, India. She has more than 10 years of research experience in nanomaterials research and more than 3 years of teaching experience. Numerous peer-reviewed journals have published her research.

three methodologies provide complementary approaches to achieve encapsulation, as illustrated schematically in Fig. 2.

2.1. *In situ* synthesis approach

It is possible to pre-embed metal ions into the pores of frameworks by connecting with framework constituent units or by using certain functional groups. Afterwards, certain conventional reducing agents can reduce those metal ions to nanoscale particles. With these *in-situ* synthesis techniques, the native crystal structure and porosity of the frameworks can be preserved.

2.1.1. Importance of reduction procedure/reducing agent. In general, conventional reducing agents such as $NaBH_4$ are used for the reduction procedure. For example, S. Kumar *et al.* synthesized Cu- and Ag-nanoparticle-modified TzTFB-COF by functionalization of the COF with $-NH_2$ groups. These $-NH_2$ groups facilitate the anchoring of Ag or Cu ions. Reduction of these ions with $NaBH_4$ leads to the formation of Cu@TzTFB-COF and Ag@TzTFB-COF, respectively, as shown in Fig. 3(a).[69] This early demonstration highlighted the feasibility of anchoring ions with functional groups, and later studies expanded the scope to a wide range of NPs@framework structures.[70,71]

The use of an external strong reducing agent, however, has a significant influence on the crystallinity and porosity of frameworks. To overcome this issue, other reducing agents have also been explored. Li *et al.* have demonstrated the efficiency of hydrogen as a reducing agent in controlling the size and position of NPs in click-based porous organic polymers (CPPs).[72] Here, $NaBH_4$ was used as a reducing agent, where Pd^{2+}@CPP-1 was converted into PdNP@CPP-1 with dual size distribution of Pd NPs, as shown in Fig. 3b and d. The interior of CPP-1 was decorated with 1.4 nm Pd NPs, while the exterior part was decorated with 3.9 nm Pd NPs. It is assumed that due to the hydrophobic nature of the polymer, aqueous $NaBH_4$ could not penetrate efficiently into the pores of CPP, and hence, some Pd ions diffuse out of the pores, leading to the formation of Pd NPs at the exterior of the pore. In contrast, when H_2 was used as a reducing agent, nucleation of Pd nanoparticles occurred within the nucleus. Growth of the nanoparticles was restricted by the polymer, resulting in uniformly distributed smaller-sized particles (~1.4 nm) as shown in Fig. 3b and c.

Beyond chemical reduction, alternative energy-assisted methods can also generate nanoparticles within frameworks. For instance, NPs can be generated inside frameworks by pyrolysis, UV radiation, or microwave irradiation. In this direction, Bhadra *et al.* developed an *in situ* approach in which Pd metal was inserted into the precursor of the COF.[73] The synthesis of Pd@TpBpy was performed by the reaction of 1,3,5-triformylphloroglucinol (Tp) with 2,2′-bipyridine-5,5′-diamine palladium chloride (Bpy-$PdCl_2$) in the presence of aqueous acetic acid and solvents. The system was heated at 90 °C, and the Pd-NPs were formed by the breakage of the Pd–N bond. Additionally, Kalidindi *et al.* demonstrated uniform distribution of smaller Pd nanoparticles (2.4 nm) by the reduction of Pd-loaded COF-102 under UV irradiation.[74]

Together, these studies highlight the importance of carefully selecting reducing conditions to control nanoparticle formation and preserve framework integrity. Similarly, innovative strategies have combined nanoparticle formation with conductive coatings. Chen *et al.* developed a unique method to form a coating of ultra-small Pd nanoparticles along with a conductive layer of poly(3,4-ethylenedioxythiophene) (PEDOT) on a hydrazone-linked COF (COF-42).[75] First, a Pd^{2+}-ions-loaded COF was synthesized by dispersing COF-42 in the H_2PdCl_4 solution. Subsequent addition of EDOT (the monomer unit of PEDOT) changed the color of the mixture from ginger brown to dark brown, indicating oxidative polymerization of EDOT monomers to PEDOT polymer and formation of Pd nanoparticles. Here, $PdCl_4^{2-}$ acted as an oxidant and was reduced to Pd NPs. The coordinating sites present in the PEDOT polymer further attracted Pd ions to deposit on the surface, resulting in uniformly distributed small-sized nanoparticles on the COF surface.

Electrochemical methods also provide alternative *in-situ* reduction routes. Pan *et al.* demonstrated an electrochemical reduction technique for the synthesis of Au nanoflower incorporated thiolated COF.[76] For this synthesis, the COF was initially modified with –SH groups. A mixture of COF-SH and carbon nanotubes was deposited on a glassy electrode, which

Rojalin Sahu

Dr. Rojalin Sahu is currently serving as a Professor of Chemistry at the Kalinga Institute of Industrial Technology (KIIT), Deemed to be University, India. She earned her M.Sc. and M.Phil. in Chemistry from Utkal University, India, and completed her Ph.D. in 2011 at the Indian Institute of Technology (IIT) Guwahati. Her research focuses on the design and development of metal–organic compounds and the investigation of their properties and potential applications. Her doctoral research was centered on the synthesis of Schiff base–based metal complexes. Dr. Sahu is a Fellow of the Royal Society of Chemistry (FRSC), one of the most prestigious recognitions conferred by the Royal Society of Chemistry (RSC). She is a recipient of the SMC Bronze Medal and the CRS Bronze Medal, and has been recognized as one of the 75 Women in STEM by the Prime Minister's Office (PMO) in collaboration with Red Dot Organization and RSC. She currently serves as an Executive Council Member of the Chemical Research Society of India (CRSI). Dr. Sahu has authored over 50 peer-reviewed research articles in reputed international journals, including ACS Nutrition Science, Chemical Communications, Nanoscale, Chemistry – An Asian Journal, CrystalEngComm, Nano Energy, Journal of Alloys and Compounds, and Chemical Engineering Journal. In addition to her research publications, she has also served as the editor of three books.

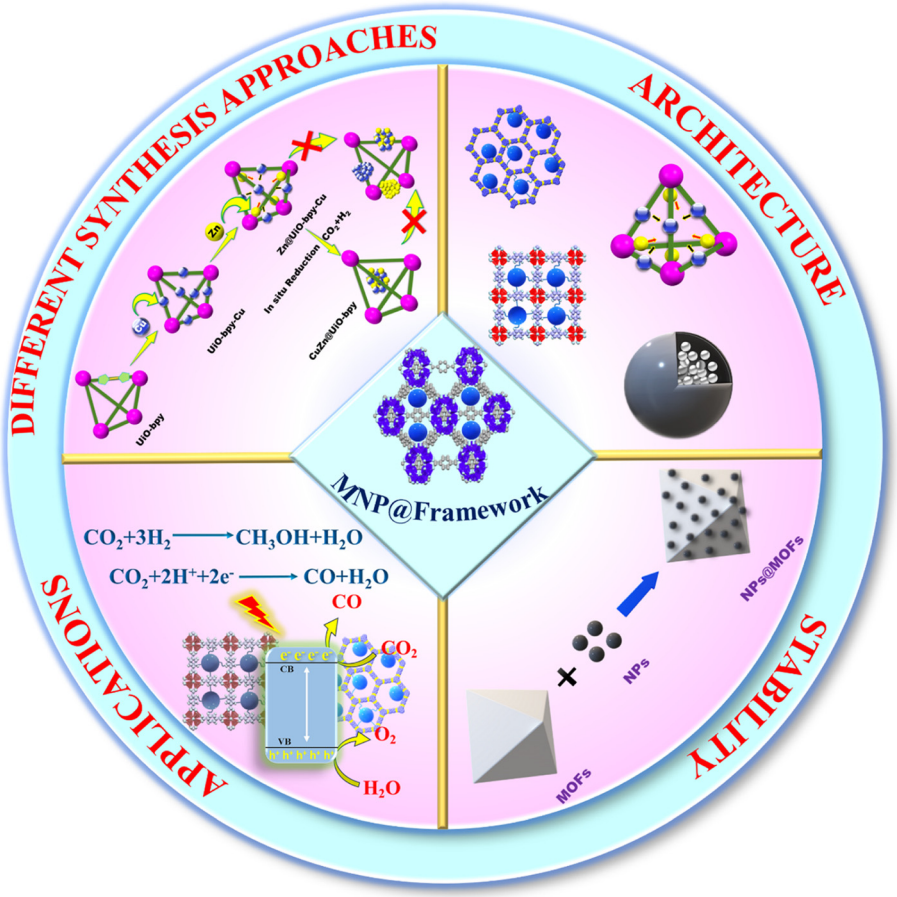

Scheme 1 Features of metal nanostructure-confined frameworks.

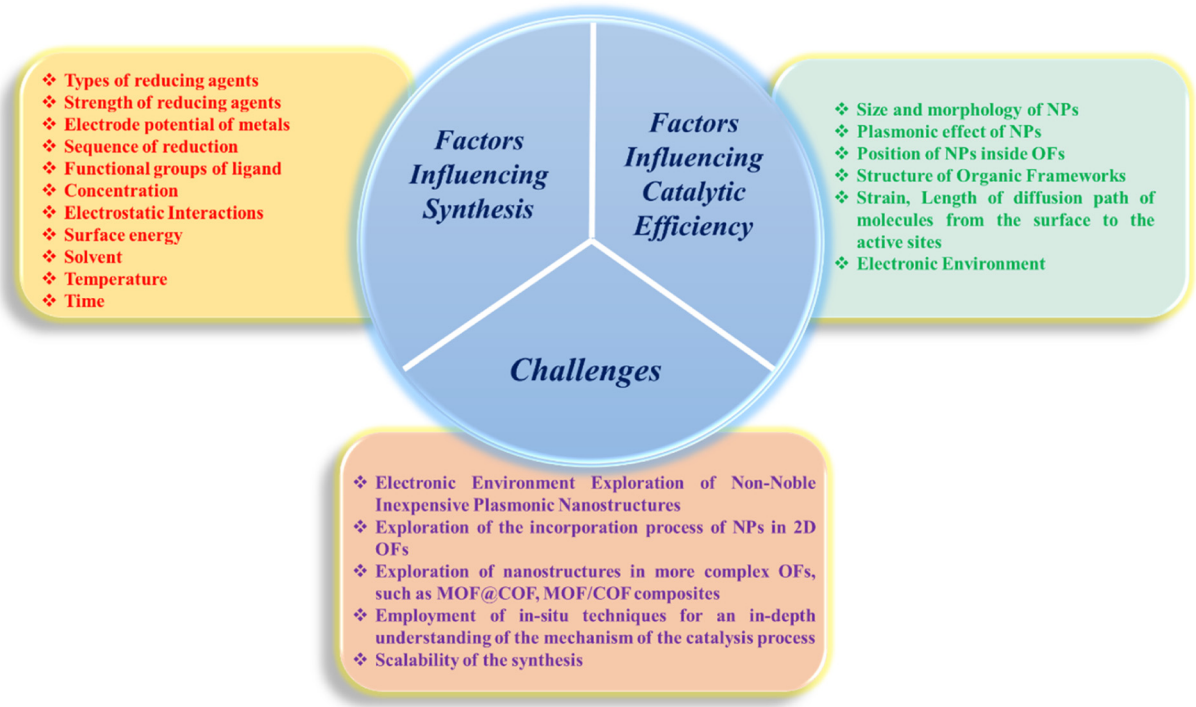

Fig. 1 Factors influencing the synthesis, catalytic efficiencies, and challenges associated with nanostructure-encapsulated frameworks.

Table 1 Comparative discussion on hybrid framework material-based literature

Sl no.	Material feature	Highlights	Ref.
1	MOF-on-MOF heterostructures	Explores interfacial engineering strategies to enhance the catalytic performance of MOF-on-MOF heterostructures	36
2	COF/MOF hybrids	Reviews progress in hybridizing COFs with MOFs to combine structural and functional advantages	37
3	MOF-derived nanocarbons and oxides	Surveys strategies for transforming MOFs into nanocarbons and metal oxide derivatives for enhanced photocatalysis	38
4	MOF–COF composites	Reviews design, synthesis, and mechanisms of MOF–COF composites for photocatalytic applications	39
5	MOFs and COFs	Provides a comprehensive overview of the status, challenges, and future prospects of MOF and COF applications	40
6	COFs	Discusses alternative synthetic methods for COFs beyond conventional solvothermal approaches	41
7	COFs for biomedical therapy	Explores COFs as rationally designed materials for targeted cancer therapy	42
8	MOFs (ML-guided discovery/ computational screening)	Demonstrates machine learning for screening MOFs, rapidly identifying candidates for photocatalytic oxygen evolution reaction (OER)	43
9	Photocatalytic MOFs	Reviews MOFs as photocatalysts for water splitting and CO_2 reduction	44
10	MOF heterojunctions	Highlights design strategies for MOF-based heterojunctions to improve charge separation and photocatalytic efficiency	45
11	COF photocatalysts	Summarises the design, linkers, morphologies, and applications of COF-based photocatalysts in energy and environment remediation	46
12	MOF-derived photocatalysts	Discusses heteroatom-doped MOF-derived materials as efficient photocatalysts for CO_2 reduction	47
13	MOF photocatalysts for CO_2 reduction	Reviews MOF-based catalysts for CO_2 reduction, focusing on mechanisms, product selectivity (CO, CH_4, C_1–C_2^+), and design strategies	48
14	Zirconium-based MOFs	Highlights defect engineering and active-site optimization in Zr-MOFs for efficient photocatalytic CO_2 reduction	49
15	MOFs, COFs, and heterojunctions	Reviews progress on MOF/COF-based photocatalysts for H_2O_2 production	50
16	COF photocatalysts	Examines COFs as tunable photocatalysts for H_2O_2 production, focusing on linker design, heterojunction, and stability	51
17	Porphyrin-based MOFs and COFs	Reviews visible-light-driven solar fuel production using nanosized porphyrin-based frameworks	52
18	MOF photocatalysts	Discusses design principles and applications of MOFs for efficient solar-driven photocatalytic water splitting	53
19	Porous organic frameworks	Demonstrates MOFs, COFs, and HOFs as multifunctional separators in rechargeable lithium metal batteries	54
20	Conductive MOFs for Zn batteries	Reviews conductive MOFs as promising electrodes for high-performance zinc-based batteries	55
21	MOF-based composites	Discusses advances in MOF composites, linking dimensionality and functionality to supercapacitor applications	56
22	COFs for biomedical implants	Reports COFs enabling NO release to enhance the multi-modal therapeutic performance of PEEK implants	57
23	Aptamer-modified MOFs	Reviews aptamer@MOF systems for efficient bacterial pathogen detection	58
24	MOFs as oxidase mimics	Discusses design and modification of MOFs to improve oxidase-mimic sensing applications	59
25	Uric acid-sensing MOFs	Reviews MOFs for uric acid detection and explores future integration with machine learning	60
26	Porphyrin MOFs and COFs	Reviews their use of heterogeneous photosensitizers for singlet oxygen-based antimicrobial nanodevices	61
27	Multiscale COF films	Develops multiscale COF films for selective sensing of multicomponent gases	62
28	Two-dimensional COFs	Reviews the design and application of 2D COFs for membrane separation	63
29	MOF/COF heterostructured hybrids	Reviews design, synthesis, and applications of MOF–COF heterostructures for advanced functions	64
30	MOF composites for photocatalysis	Reviews classifications and synergistic design of MOF composites, including metal/MOF systems	65
31	Noble-metal/MOF photocatalysts	Summarises synergistic effects of noble metal nanoparticles in MOF photocatalysis	66
32	Encapsulated metal NPs in porous hosts	Summarises advances in the synthesis and catalysis of encapsulated metal NPs in porous supports, emphasizing stability, selectivity, and metal–support interactions	67
33	MOF-based photocatalysts for CO_2 reduction	Summarises recent developments in MOF-based photocatalysts including NP-loaded systems	68
34	Metal nanocluster-confined reticular materials	This review critically analyzes various factors influencing synthesis strategies, stabilization of metallic nanostructures and discusses the synergistic effects of nanoparticles and organic frameworks on photocatalytic applications. To the best of our knowledge, this is the only review that critically analyses and correlates factors influencing synthesis and activity	This review

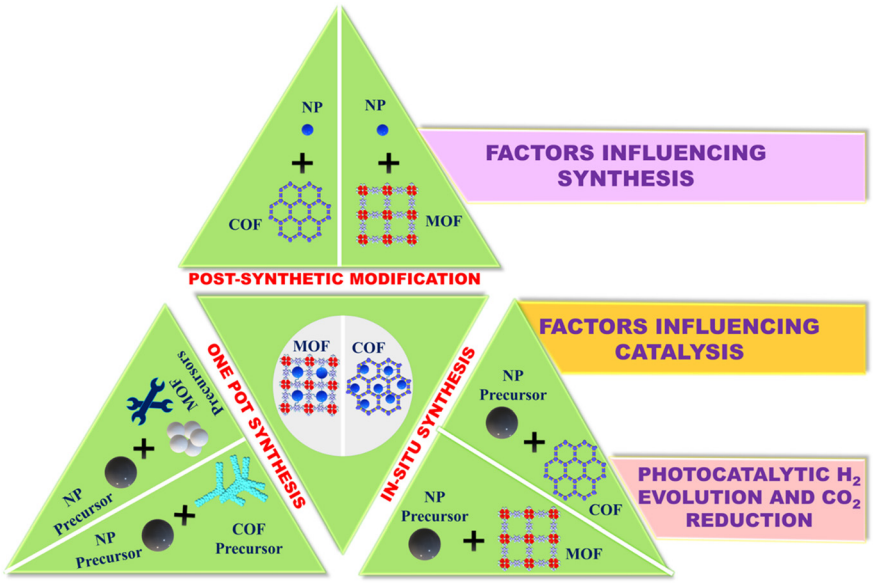

Fig. 2 Illustration of the synthesis method for framework-encapsulated nanostructures.

was then dipped in a 1 mM solution of $HAuCl_4$. A nanoflower-decorated COF-SH/CNT was formed at a potential of −0.2 V for 60 s.

Interestingly, the sequence of reduction also influences the final structure of bimetallic NP-encapsulated frameworks. Pan *et al.* showed that simultaneous reduction of $HAuCl_4$ and H_2PtCl_6 led to randomly distributed Pt and Au nanoparticles inside UiO-66 MOF.[77] However, sequence addition produced different architectures: when $HAuCl_4$ was added to Pt@UiO-66, followed by $NaBH_4$ reduction, a composite structure formed with Pt nanoparticles at the core and Au nanoparticles distributed inside the MOFs. Similarly, when Ag^+ ions were impregnated and reduced in Au@ZIF-8, it led to the formation of Au@Ag@ZIF-8. However, reversing the order, *i.e.*, addition of Au^+ ions to Ag@ZIF-8, followed by reduction, yielded Au@AuAg@ZIF-8. This difference arises from the reduction potentials of metals. Compared to Ag^+/Ag, Au^{3+}/Au has a greater reduction potential and hence when Au^{3+} is added to Ag@ZIF-8, part of the Ag metal is utilized in the reduction process of Au^{3+} ions, and the remaining Ag^+ ions and Au^{3+} ions form an AuAg alloy shell *via* co-reduction, as shown in Fig. 3e.[78]

The strength of the reducing agents also plays a critical role in determining NP structure. Chen *et al.* demonstrated this using Pd- and Co-ion-impregnated MIL-101. Interestingly, the use of a strong reducing agent such as $NaBH_4$ led to the formation of PdCo alloy nanoparticles encapsulated in MIL-101. In contrast, using aminoborane (a weaker reducing agent) led to the formation of Pd@Co core–shell nanoparticles inside MIL-101, as shown in Fig. 3f.[79] A similar strategy was adopted by Xie *et al.* to prepare an Au nanoneedle@zirconium-based porous coordination network (AuNN@PCN-222).[80] Here, Au^{3+} ions were reduced by carboxylate ions present in the framework. However, reduction with $NaBH_4$ resulted in the formation of Au NPs on the surface of PCN-222, as shown in Fig. 3g. This was attributed to slower reduction with carboxylate ions, which allowed crystallization of Au nanoneedles (NNs), while rapid reduction by $NaBH_4$ triggered multiple nucleation events leading to the formation of nanoparticles. The larger diameter of Au NNs compared to the pore channel indicated partial framework erosion due to node–linker linkage.

Difference in reduction potential can also be exploited to develop a series of bimetallic alloy NPs inside the frameworks. According to Chen *et al.*, under high-intensity ultrasonic irradiation, transition-metal NPs (Cu, Co, Ni) can undergo galvanic exchange with noble-metal ions (Pd, Ru, Pt), producing ultrafine alloy NPs within MIL-101, as illustrated in Fig. 3h. Ultrasonic irradiation initiated galvanic replacement reactions, yielding alloys such as CuPd, CuRu, CuPt, CoPd, CoRu, CoPt, NiPd, NiRu, and NiPt were formed using this protocol.[20,82]

Additionally, the precursor addition procedure influences final NP morphology. Hermannsdörfer *et al.* showed that bimetallic Ni/Pd nanoparticles could be formed by reducing Ni and Pd precursors loaded into an MIL-101 MOF. When both precursors were loaded simultaneously, smaller nanostructures resulted, as shown in Fig. 3j. Conversely, larger Pd nanostructures were formed when Ni precursor was loaded after Pd nanostructure formation, as shown in Fig. 3i.[81] In this case, aminoborane reduced Pd^{2+} (with higher reduction potential than Co^{2+}), while Co^{2+} ions were subsequently reduced by M–H species generated during the hydrolysis of the reducing agent.

2.1.2. Site-directed reduction strategy. As explained above, metals present in MOFs can be reduced to produce nanostructure-encapsulated frameworks. If a MOF contains more than one type of metal, preferential reduction of one metal over another can occur depending on the reduction potential. This strategy helps in controlling the spatial distribution and structural arrangement of nanostructures within the frameworks. In this context, Bai *et al.* calculated the reduction potential for different MOFs and found that it

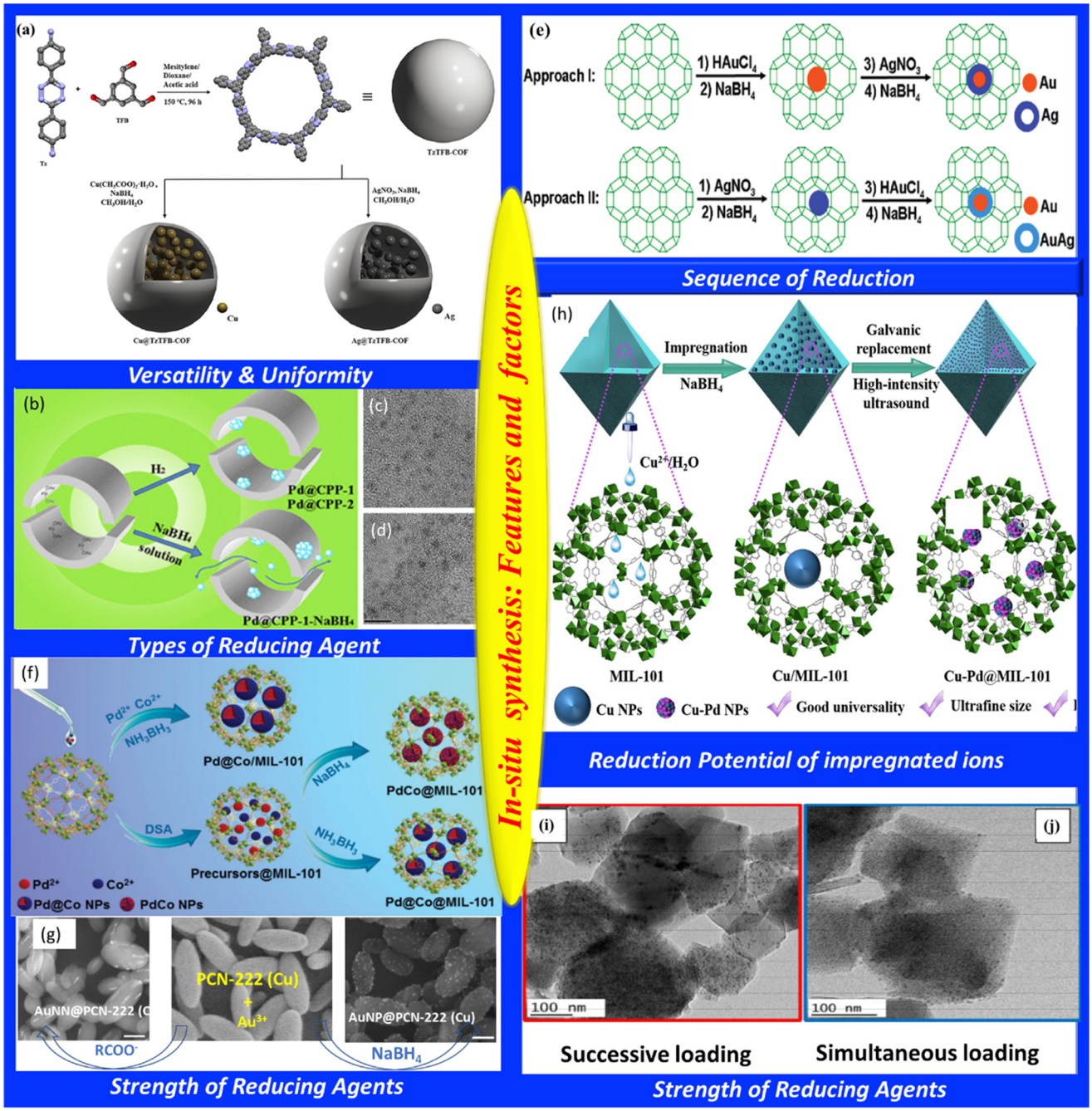

Fig. 3 (a) Diagrammatic illustration of TzTFB-COF formation and functionalization with Ag and Cu NPs. Adapted from ref. 69, with permission from the American Chemical Society, copyright 2023. (b) Diagrammatic illustration of the synthesis of Pd@CPP with different reducing agents. (c and d) TEM images of Pd@CPP obtained by reduction with H_2 and $NaBH_4$ respectively. Adapted from ref. 72, with permission from the American Chemical Society, copyright 2014. (e) Schematic of synthesis procedure of Au@Ag@ZIF-8 and Au@AuAg@ZIF-8. Adapted from ref. 78, with permission from the American Chemical Society, copyright 2011. (f) Synthesis of Pd@Co@MIL-101, Pd@Co/MIL-101, and PdCo@MIL-10 catalysts by different procedures and reducing agents. Adapted from ref. 79, with permission from Wiley, copyright 2014. (g) TEM images of PCN-222 (Cu), AuNN@PCN-222 (Cu) and AuNP@PCN-222 (Cu). Adapted from ref. 80, with permission from Nature, copyright 2022. (h) Schematic of synthesis procedure of Cu–Pd NPs@MIL-101.[82] Adapted from ref. 82, with permission from the American Chemical Society, copyright 2019. (i and j) TEM images of $Pd_{2.5}Ni_{2.5}$@MIL-101. Slightly bigger metal NPs are obtained by successive loading of Pd and Ni. Simultaneous loading results in smaller NPs within MIL-101. Adapted from ref. 81, with permission from Wiley, copyright 2012.

primarily depends on the metal center and is only slightly affected by the framework.[83] They prepared a core–shell structure of two different MOFs, in which the core or the shell acted as the active component and was reduced with the help of $NaBH_4$. For example, in the core–shell structure of ZIF-67@ZIF-8 and Cu-HKUST-1@Zn-HKUST-13, the active cores (ZIF-67 and Cu-HKUST-1) were reduced to metal nanostructures, while the shells remained intact. This led to the formation of MOF@MOF

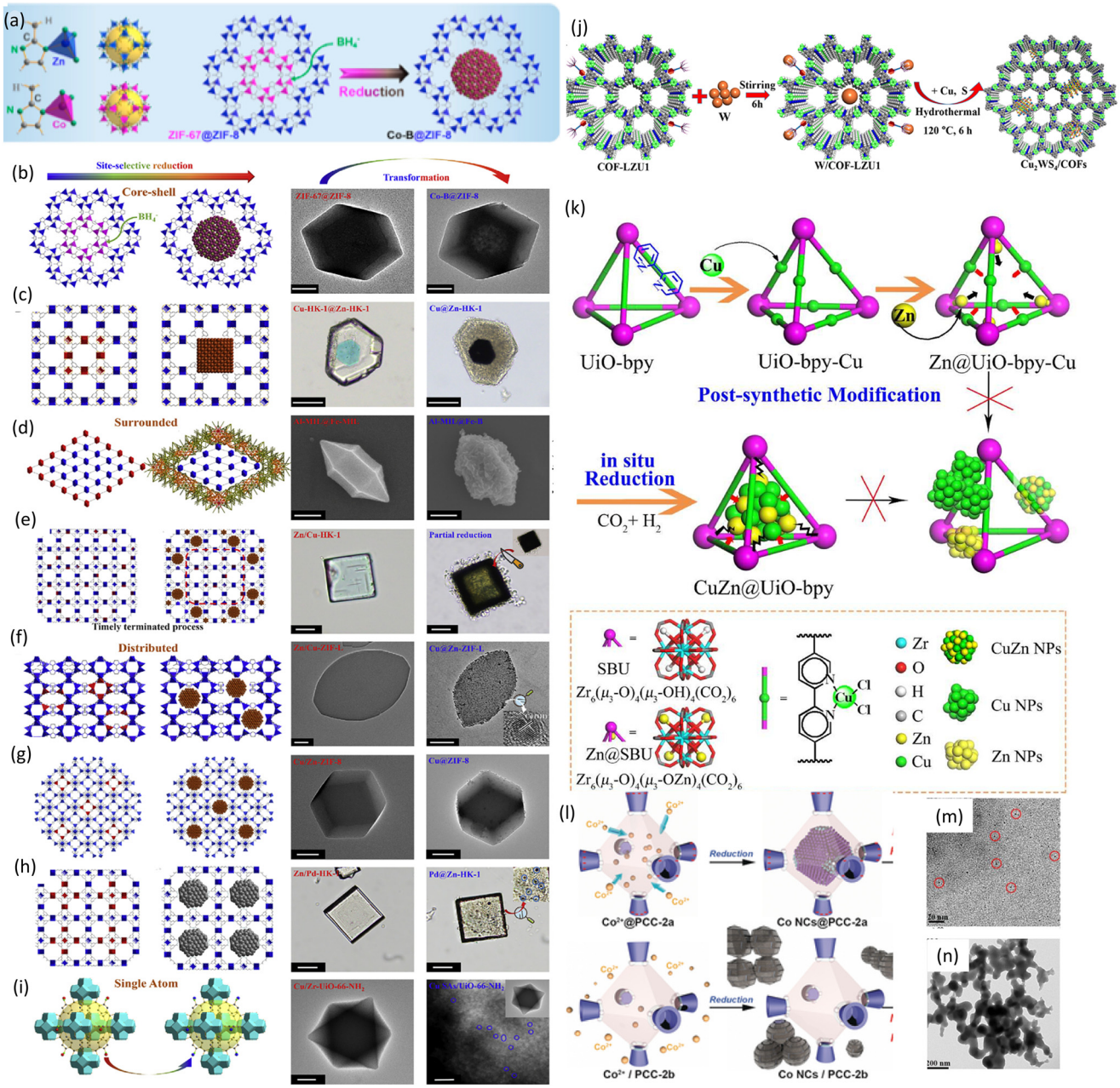

Fig. 4 (a) Zn-MeIM and Co-MeIM coordination mode in ZIF-8 and ZIF-67, where the tetrahedrons represent primary building units in ZIFs. Left: change in crystal structure during the process of constructing the yolk–shell structure. Adapted from ref. 83, with permission from Elsevier, copyright 2021. Schematic drawings of crystal structure transformation, morphology changes (SEM, TEM, scanning TEM, or optical microscope images) of (b) ZIF-67@ZIF-8, (c) Cu-HKUST-1@Zn-HKUST-1, (d) Al-MIL-53@Fe-MIL-53 (scale bars: 300 nm), (e) Zn/Cu-HKUST-1 (scale bars: 50 mm), (f) Cu/Zn-ZIF-L (scale bars: 400 nm), (g) Cu/Zn-ZIF-8 (scale bars: 100 nm), (h) Zn/Pd-HKUST-1, and (i) Cu/Zr-UiO-66-NH_2. Adapted from ref. 83, with permission from Elsevier, copyright 2021. (j) Schematic representation of the synthesis of the Cu_2WS_4 nano-homojunction@COF hybrid material.[100] Adapted from ref. 100, with permission from the American Chemical Society, copyright 2022. (k) Synthesis of CuZn@UiO-bpy through *in situ* reduction of post-synthetically metalated UiO-bpy. Cu^{2+} ions were coordinated to the bpy groups while Zn^{2+} ions were attached to the SBUs. Adapted from ref. 93, with permission from the American Chemical Society, copyright 2017. (l) The 6-anionic PCC-2b hardly encapsulates metal cluster precursors, by showing bulky and aggregated nanoclusters. The highly reactive Co nanoclusters encapsulated by PCC-2a, show considerable activity improvement for the hydrolysis of ammonia borane. (m and n) TEM images of Co NCs@PCC-2a (red cycles indicate single NCs) and Co NCs/PCC-2b.[101] Adapted from ref. 101, with permission from Wiley, copyright 2018.

core–shell structures into a metal NP@MOF yolk–shell structure. Interestingly, if the metal present in the shell has a higher reduction potential, selective reduction occurs in the shell. For instance, in MIL-53(Al)@MIL-53, Fe is reduced, resulting in a crystalline core (MIL-53(Al)) surrounded by an amorphous Fe–B alloy, as shown in Fig. 4a. This strategy has been extended to obtain a wide variety of NP@framework structures, as shown in Fig. 4b–i.

The duration of reduction is another important factor. Timely reduction of Cu/Zn bimetallic MOFs results in the reduction of Cu clusters in the outer layer, producing a quasi-core–shell structure (Fig. 4e). Similarly, selective reduction of Cu ions in evenly distributed bimetallic MOFs such as Cu/Zn-ZIF-L and Cu/Zn-ZIF-8 leads to the formation of evenly dispersed Cu nanostructures encapsulated within MOFs, as shown in Fig. 4f. These examples confirm the general utility of site-selective strategies for forming metal nanostructures enclosed in MOFs. Reduction efficiency and the resultant structure also depend on the strength of the reducing agent, which can be tuned by the use of different solvents. For example, site-selective reduction of ZIF-67@ZIF-8 with $NaBH_4$ dissolved in an ethanol–water mixture produced intact MOF–metal composites. However, when $NaBH_4$ was used in water alone, it acted as a powerful reducing agent, completely disintegrating the ZIF-8 shell and leaving only the Co–B core. However, the mixture of water with $NaBH_4$ controlled the reduction process.

2.1.3. Influence of solvent. Solvents have a strong influence on the encapsulation of NPs inside frameworks. A double solvent approach is commonly used to avoid aggregation of NPs on the outer layer of frameworks. In this process, metal precursors are dissolved in a significant volume of hydrophobic solvent, such as hexane, and a small amount of hydrophilic solvent, like water. The volume of the hydrophilic solvent is less than the pore volume of the frameworks. As the internal surface area of frameworks is much higher than the external surface area, metal precursors in hydrophilic solvents penetrate the core by capillary forces. Subsequent reduction of these precursors leads to encapsulation of NPs inside the frameworks.[84–86] The solvent also significantly influences NP size and location.

For instance, Tao *et al.* investigated solvent effects on the growth of Pd NPs inside a triangular bipyramid covalent organic cage (Phos-cage) containing two triphenylphosphine and three diamine moieties. They dispersed Phos-cage and K_2PdCl_4 in solvents such as pyridine, THF, and methanol and reduced with $NaBH_4$. In pyridine, larger Pd nanoparticles (~3.39 nm) were obtained compared to THF (~1.19 nm) and methanol (~0.85 nm). Pyridine has a stronger affinity towards Pd, and faster ligand exchange between Cl^- of $[PdCl_4]^{2-}$ occurs, leading to the formation of a large pyridine–Pd complex. The complex could not enter the pore of the core, and successive reduction leads to the formation of Pd nanoparticles outside the core. Methanol has low coordination ability with Pd and does not affect the entry of $[PdCl_4]^{2-}$ inside the cage. Hence, smaller NPs were formed inside the cage after reduction.[87]

2.1.4. Influence of functional group. Functional groups in frameworks strongly affect NP formation since they bind precursor ions. For example, Pan *et al.* have encapsulated Au nanoflowers within COFs by electrochemical deposition.[76] COFs were functionalized with –SH using three different ligands, namely 2,3-butanedithiol, 1,2-ethanedithiol, and methyl mercaptan. The corresponding pore sizes were 28.5, 24.6, and 27.9 Å, while the interlayer spacing was 3.77, 3.87, and 3.52 Å, respectively. The observation thus confirms that the COFs modified with 2,3-butanedithiol had a higher interlayer spacing and a relatively modest pore size. This indicates comparatively denser attachment sites of 2,3-butanedithiol with the same specific surface area. This condition is favored for the attachment of Au nanoflowers on COF–SH. N content in the framework also influences the nanostructure size and stability.

Nitrogen functionalization can also stabilize NPs. For instance, Jiang *et al.* reported that nitrogen-rich covalent organic frameworks can control the local Pd nanoparticle environment to achieve selective semi-hydrogenation of alkynes.[88] In this work, high Pd–N coordination and framework confinement were used to control Pd dispersion and electronic structure. Lan *et al.* showed that exfoliation of CTFs exposed more nitrogen groups, which stabilized Ag NPs.[89] Ultrafine Ag NPs were embedded by adding $AgNO_3$ precursor to exfoliated CTF nanosheets, followed by reduction with $NaBH_4$. XPS analysis confirmed N–Ag coordination as the stabilizing mechanism.

Similarly, sulfur-based functionalization enables ultrafine NP growth. Lu *et al.* proposed an innovative strategy utilizing COFs as templates for the controlled synthesis of ultrafine, stable, and well-dispersed metal NPs. They designed and synthesized a thioether-functionalized COF to confine the growth of metal NPs. The uniform distribution of thioether groups within the ordered framework facilitated the formation of platinum (Pt) and palladium (Pd) nanoparticles averaging 1.7 ± 0.2 nm in size, exhibiting a narrow size distribution. This was achieved by impregnating the COF with K_2PtCl_4 and K_2PdCl_4, followed by reduction using $NaBH_4$. A similar process with the same crystalline COF but without thioether groups leads to the formation of both small and aggregated Pt/Pd NPs inside frameworks.[90] Further, Mishra *et al.* have developed a novel thiol-functionalized MOF as a template for the controlled synthesis of highly dispersed ultrafine yet stable ruthenium (Ru) nanoparticles. They have shown that the Ru NPs of 1.5 nm size are well stabilized with thiol-functionalized Ni-MOF.[91]

Beyond stabilization, functional groups can direct precursor incorporation. Chen *et al.* incorporated Pd ions into UiO-67 using 2,2-bipyridine-5,5′-dicarboxylic acid as a ligand, which acted as an anchoring site due to its structural similarity to biphenyl dicarboxylic acid (the native UiO-67 linker). Reduction with H_2 yielded Pd NPs.[92] Similarly, Wang *et al.* synthesized defect-rich Cu_2WS_4@COF by pre-anchoring W ions in COF-LZU1, followed by hydrothermal treatment with $CuCl_2$ and thioacetamide. The synthesis procedure is shown in Fig. 4j.[35,100]

Bimetallic nanostructures within frameworks are formed through a strong interaction between metal ions and the functional group of frameworks. Lin *et al.* demonstrated this by synthesizing ultra-small Cu/ZnO_x NPs on preassembled bpy and $Zr_6(\mu_3\text{-}O)_4(\mu_3\text{-}OH)_4$ sites in UiO-bpy.[93] Here, for the formation of Cu/ZnO_x NPs, Cu^{2+} ions were first coordinated

onto the bpy sites present in MOF by post-synthetic metalation with $CuCl_2$, followed by the introduction of Zn^{2+} ions by reaction with $ZnEt_2$ with the μ_3-OH sites on the SBUs. Reduction of these ions with H_2 at 250 °C leads to the formation of ultra-small Cu/ZnO_x NPs (1 nm) within the MOF, as shown in Fig. 4k. The robust interactions between Cu/ZnO_x NPs and the bpy groups of the ligands as well as Zr_6 SBUs stabilize these ultra-small NPs, preventing their agglomeration and phase separation between Cu and ZnO_x.

Similarly, Ding *et al.* have shown that diamine-containing UiO-66 (UiO-66-$(NH_2)_2$) can effectively coordinate with the precursor of Pd/Au NPs during the preparation and hence result in smaller-sized particles.[94] These UiO-66-$(NH_2)_2$ also efficiently stabilized the PdAu NPs during the catalysis process compared to UiO-66-NH_2, thereby significantly accelerating the dehydrogenation of formic acid.

2.1.5. Influence of metal nanoparticles. The presence of one NP can influence the deposition of others in bimetallic nanoparticle formation. Chen *et al.* fabricated core–shell bimetallic Pd@Ag NPs within the pores of UiO-67 MOF.[95] First, Pd NPs were encapsulated, then treated with H_2. It is known that H_2 can be dissociated into atomic hydrogen and spill over onto the Pd sites embedded within the MOF structure.[96] These atomic hydrogens reduce Ag^+ ions, leading to the formation of Pd@Ag@UiO-67 structures. This procedure works for a range of concentrations of Pd and Ag.

2.1.6. Electrostatic interaction. Electrostatic interactions also play a major role in the NP encapsulation process in frameworks. Fang *et al.* showed that the charge on the frameworks can be modulated in order to efficiently incorporate metal nanoparticles inside.[36,101] Co^{2+} ions were incorporated into soluble porous organic cages PCC-2a and 2b, as shown in Fig. 4l. Both PCC-2a and 2b have similar structures. However, PCC-2a has five times more negative charge than PCC-2b and hence can absorb metal ions efficiently. Reduction of these ions leads to the formation of nanoparticle-encapsulated porous organic cages. However, as Co^{2+} ions are not effectively absorbed by PCC-2b, hence the reduction of these ions also leads to the formation of nanoparticles outside the porous cages. Yang *et al.* demonstrated fine control over the size of encapsulated NPs by controlling the electrostatic interaction.[97] Sub-nm to 2 nm NPs of Cu, Pd, and Pt were encapsulated within a Zr-based MOF, NU-1000. The pH of the solution was varied to control electrostatic interactions.

2.1.7. Impact of temperature. Pyrolysis of MOFs also leads to the reduction of metal ions, leading to the formation of MOFs. However, pyrolysis temperature must be optimized to prevent degradation of MOFs. Cui *et al.* have demonstrated formation of the Co/MnO_x nanostructure encapsulated quasi-MOF-74 by controlled pyrolysis of CoMn-MOF-74.[98] It was confirmed from TGA analysis that at 400 °C, terephthalate ligands were partially decomposed into some reducing agents, leading to the formation of the Co/MnO_x nanostructure. Above 400 °C, complete decomposition of organic ligands occurred. Shen *et al.* further demonstrated that pyrolysis temperature dictates NP morphology.[99] When CuCo-bimetallic MOF was pyrolyzed, Cu nanoparticles began to form at 260 °C, and Cu-nanowire encapsulated quasi-MOFs were formed at 300 °C. Aggregated Cu nanoparticles@quasi-MOFs were formed at 340 °C (Fig. 4m and n). Owing to the difference in metal-ligand bond stability, the Cu^{2+} coordination bonds decomposed prior to those Co^{2+} during pyrolysis, leading to the preferential reduction of Cu^{2+} by carbonaceous species formed from ligand decomposition. They also showed that the formation of this specific Cu nanowire@quasi-MOF structure depends on the presence of Co ions in the framework. Under similar conditions of pyrolysis, Cu-MOFs transformed into yolk–shell structures with aggregated Cu nanoparticles at the center. Pyrolysis of CuNi MOFs results in the formation of Cu and Ni nanoparticle-encapsulated quasi-MOFs, while pyrolysis of CoCu MOFs results in the formation of Cu nanowire-encapsulated quasi-MOFs. The underlying mechanism still requires investigation.

2.1.8. Influence of time. Time brings significant changes in the metal nanostructure encapsulated frameworks. Chen *et al.* have shown a generic way to prepare alloy nanoparticle-encapsulated MIL-101 as described above.[82] Upon addition of Pd^{2+} ions, the Cu@MIL-101 framework underwent a time-dependent structural evolution, gradually converting into CuPd alloy nanoparticle-encapsulated MIL-101. Formation of alloy nanoparticles started with the formation of core–shell nanoparticles within 30 s, formed by the galvanic displacement of surface Cu atoms by Pd^{2+} ions. With further irradiation, the aggregates reorganized into more stable alloyed NPs (Table 2).

2.2. Post-synthesis approach

Compared to the *in situ* synthesis method, this approach avoids the issues associated with nanostructure formation on the external surface of the frameworks and the structural damage of frameworks arising from impregnation reduction. This method offers the benefit of incorporating metal nanostructures with different sizes, shapes, and compositions. For example, ZIF-8 MOFs can be grown on the hollow TiO_2 NP surface using a sonochemical approach.[107]

However, this approach often relies on trial-and-error optimization. Harsh conditions, such as high temperature and low pH, can accelerate aggregation of nanostructures. Moreover, it is difficult to place nanoparticles uniformly inside each framework, resulting in a low yield of nanostructure-encapsulated frameworks in self-assembled structures. This approach has been adopted for confining nanostructures within different types of frameworks such as MOFs and COFs. Additionally, it has also been extended to organic molecular cages (OMCs). For instance, Inomata *et al.* recently demonstrated that thiolate-protected Au_{55} clusters, Grubbs's second-generation ruthenium catalysts, and zinc *meso*-tetraaryl porphyrins may be directly mixed to encapsulate Au_{55} clusters in hexaporphyrin cages in a controlled manner.[54] Through the cage pores, tiny substrates can reach the Au_{55} cluster cores.

2.2.1. Importance of ligands. Ligands influence the encapsulation process in many ways. Zhou *et al.* investigated the importance of ligand concentration on encapsulation

Table 2 Compilation of reported methods for the *in situ* synthesis of framework-encapsulated nanostructures

Nanostructure precursor	Framework	Resultant structure	Approach adopted	Important observation	Ref.
$HAuCl_4$ $PdCl_2$	Cu-MOF	Au–Pd decorated Cu-MOF	Reduction with $NaBH_4$	Cu^{2+} ions present in the MOF are not reduced	102
$AgNO_3$	CTFs	Ag^0@CTF nanosheets	Exfoliation of CTFs followed by reduction with $NaBH_4$	Exfoliation of CTFs enhances	89
$HAuCl_4$	COF	Au nanoflower/SH–COF/CNTs	Electrochemical reduction	Functional group influences the resultant structure	76
Co–Mn metal within MOF	CoMn-MOF-74	Co/MnO_x nanoparticle-encapsulated quasi-MOF	Controlled pyrolysis	By carefully deligandating CoMn-MOF-74, the Co/MnO_x NPs were *in situ* enclosed within quasi-MOF-74	98
Cu present within MOF	CuCo-MOF	Cu nanowire-encapsulated quasi-MOF	Controlled pyrolysis (300 °C, N_2 atmosphere)	Mild pyrolysis retains framework integrity while forming *in situ* Cu nanowires, enhancing catalytic oxidation efficiency	99
Pd present in 2UiO-67 framework	UiO-67	Pt NPs@UiO-67	Reduction by solvent molecules at high temperature (130 °C)	N atoms present in the OF stabilize the Pd NPs	103
Copper(II) nitrate hydrate and palladium(II) nitrate hydrate	MIL-101	2–3 nm Cu, Pd, and Cu–Pd alloy nanoparticles are encapsulated in MIL-101	Microwave irradiation	Microwave irradiation simultaneously activates the pores of MIL-101 and reduces metal ions	104
Chloroauric acid H_2PtCl_6	UiO-66	UiO-66 having uniform distribution of Pt- and Au-nanoparticles UiO-66 having Pt-NPs at the center and Au-NP distributed inside MOF	Simultaneous and sequential reduction with $NaBH_4$	The sequence of nanoparticle addition and reduction influences the final structure	77
$AuCl_3$, $PdCl_2$, Pd $(OAc)_2$	MOF-253	Au–Pd@MOF-253	Sequential deposition and reduction (with H_2) of Au and Pd on MOF-253	Selectivity for the carbonylation of amines was obtained by Au–Pd/MOF catalysts through adjusting the molar ratio of Au and Pd	105
K_2PtCl_4 $SnCl_2{\cdot}2H_2O$	UiO-66-NH_2	Pt–Sn alloy encapsulated within UiO-66-NH_2	Sequential impregnation of Pt and Sn, followed by reduction with H_2	Control over Pt and Sn concentration can be achieved by sequential impregnation	106
$Pd(NO_3)_2{\cdot}2H_2O$ $CoCl_2{\cdot}6H_2O$	MIL-101	PdCo alloy@MIL-101 Pd@Co core–shell@MIL-101	Reduction with aminoborane Reduction with sodium borohydride	Electrochemical reduction potential difference between two metals leads to the formation of a core–shell structure with a weak reducing agent	79
$CuCl_2{\cdot}2H_2O$ $PdCl_2$ $RuCl_3{\cdot}xH_2O$ $Pt(NO_3)_2$	MIL-101	CuPd, CuRu, CuPt, CoPd, CoRu, CoPt, NiPd, NiRu, and NiPt@MIL-101	Galvanic replacement	Electrochemical reduction potential difference between two metals	82
$Pt(NO_3)_2{\cdot}2H_2O$ $AgNO_3$	MIL-101	PdAg@MIL-101	Double-solvent approach	Very small PdAg alloy NPs (~1.5 nm) have been encapsulated into MIL-101	86
Et_3PAuCl	NU-1000	Au@NU-1000	Modification of MOF to bind specific Au(I) phosphine, followed by condensed phase reduction	Pore size of MOF controls the size of NPs	2
$CuCl_2$ $ZnEt_2$	UiO-bpy	$CuZnO_x$@UiO-bpy	*In situ* reduction during CO_2 hydrogenation	Strong interactions between Cu/ZnO_x NPs and the bpy groups of the ligands and Zr_6 SBUs stabilize these very small NPs	93
$HAuCl_4$	PCN-222 (Cu)	Au nanoneedle@ PCN-222 (Cu)	Impregnation of Au^{3+} ions followed by electronic activation of N sites within the Cu-porphyrin MOF	Reduction with $-RCOO^-$ leads to the formation of AuNN@PCN-222 (Cu), and reduction with $NaBH_4$ leads to the formation of AuNPs on the surface of PCN-222 (Cu)	80

efficiency.[108] They synthesized PVP-capped Pt nanoparticles with low, medium, and high PVP content (termed LoP, MoP, and HiP, respectively), and encapsulated them within UiO-66 MOFs. It was found that LoP were well encapsulated, while encapsulation efficiency decreased with increasing ligand concentration. This difference was attributed to NP surface energy – LoP had higher surface energy and thus attached more strongly to MOF units during self-assembly.

However, this principle is not universal. Some nanostructures require a specific number of ligands for stability, and their dimensionality also depends strongly on ligand concentration. Yang *et al.* showed that altering ligand concentration can even affect the location of metal NPs.[109] When Au nanoparticles anchored on ZnO nanorods were dispersed in DMF/H_2O containing 2-methylimidazole (Hmim) and kept at 70 °C for 12 h, the formation of ZnO@Au@ZIF-8 resulted. At low concentrations, Hmim reacted with Zn^{2+} ions at the surface of ZnO, producing ZnO@Au@ZIF-8 with Au NPs located on the surface. At high concentrations of Hmim, Au NPs were embedded inside the MOF shell.

This ligand concentration-dependent positioning of metal nanoparticles can be attributed to two distinct formation mechanisms.[110] At high ligand concentrations, the dissolution–precipitation mechanism, as shown in Fig. 5a, is operative, wherein parent oxides dissolve to yield metal ions into solution, followed by the nucleation and growth of MOFs. During this process, metal nanoparticles become immobilised at the oxide–MOF interface and are subsequently embedded within the MOF matrix as crystallisation proceeds. Conversely, under the localised conversion mechanism, as shown in Fig. 5b, where insoluble oxide or hydroxide precursors are directly converted into MOFs through acid–base interactions, with no ion release into solution. In this case, metal nanoparticles are positioned near the MOF surface rather than being entrapped within the framework. Time-dependent structural evolution corresponding to each mechanism is shown in Fig. 5c–h and Fig. 5i and j, respectively.

Building on this, Chen *et al.* have demonstrated a dual-ligand strategy to create NP-COF heterostructures (Fig. 5k–m).[111] SiO_2 NPs were first modified with PEI and PVP, followed by addition of COF precursors, 1,3,5-triformylbenzene (TFB) and 1,4-phenylenediamine (PDA). Two competitive reactions occurred: (i) homogenous nucleation, leading to COF NP formation, and ii) heterogeneous nucleation, forming SiO_2@COF. The critical concentration for homogeneous nucleation (C_5) is fixed for a particular condition, but for heterogeneous nucleation depends on the surface properties. Critical concentration for heterogeneous nucleation (C_4) on a naked SiO_2 surface is the same or even higher than that of homogeneous nucleation. When NPs were modified with PEI, Schiff base reaction accelerated the deposition of COF precursors on the surfaces of NPs, lowering the critical nucleation concentration. However, too-fast growth of the COF resulted in a non-uniform shell. When NPs' surfaces were coated with PVP, COF precursors prefer to deposit on the surfaces of NPs because of the H-bonding. This process is much slower than with PEI. The concentration of PVP and PEI can be varied to control the rate of the reaction and, hence, the shell thickness and uniformity.

The positioning of metal NPs within the MOF layers can be controlled by adjusting the crystallization process of the MOFs through varying the concentration of organic ligands. Acharya *et al.* developed a unique strategy to create a skin-like thin layer of COF on the surface of plasmonic Ag nanoparticles coated with hollow silica.[4] Hollow silica helped to keep Ag nanocrystals separated, which made the surface of these nanocrystals accessible. These h-SiO_2-capped Ag nanocrystals were immersed in a solution containing diol (DAL, 1,4-benzenedimethanol) and triamine [TAE, 1,3,5-tris(4-aminophenyl)benzene]. Exposure of this solution to a blue laser of 405 nm for 1 h led to the formation of a thin coating of COF on the surface of Ag nanocrystals. With the help of ^{1}H NMR, it was proven that the surface of Ag nanoparticles helped in the oxidation of DAL to dialdehyde upon laser irradiation, and a COF layer was formed by the aldehyde–amine condensation-crosslinking reactions. However, direct condensation of aldehyde and amine on the Ag@h-SiO_2 surface led to the formation of a bulk COF layer around Ag@h-SiO_2. Replacement of light with heat also does not lead to the formation of a thin layer.

Coordination of ligands with metals also controls the NP–framework heterostructure. Li *et al.* used a Pt–Ni frame as a sacrificial template for the growth of Pt–Ni@Ni-MOF-74. Ni^{2+} ions formed after reaction of Ni^0 with oxygen diffused outward and were captured by MOF precursors, forming Pt-enriched Pt–Ni@Ni-MOF-74, as shown in Fig. 5n–q. Similarly, Chen *et al.* demonstrated that selective etching of Co^{2+} from an alloy by ligands results in a ternary alloy encapsulated by different MOFs.[112] RhCoNi nanoflowers (NFs) were used as a sacrificial component. Solvothermal treatment of RhCoNi NFs with 2-methylimidazole (HmIM) led to preferential etching of Co^{2+} ions. These ions reacted with HmIM to form ZIF-67 (Co) MOF. In a subsequent step, repetition of the same process with 2,5-dihydroxyterephthalic acid (DOT) resulted in the formation of MOF-74(Ni)-encapsulated RhCoNi NFs owing to the stronger coordination ability of Co^{2+} ions with DOT.

In addition to etching strategies, organic modulators can also be employed to tune NP@MOF growth. Organic molecules act as modulators and strongly influence the size and uniformity of NP@MOF. Wang *et al.* demonstrated that controlling the nucleation rate using modulators can regulate the crystal size of MOFs. Specifically, they synthesized Pt- and Pd-encapsulated MOFs using acetic acid as a modulator.[113] Acetic acid competed with dicarboxylic linkers to react with zirconium ions (Zr^{4+}) during the nucleation and growth of NP@UiO-66, thereby providing control over particle size.

2.2.2. Impact of size/surface energy. Zhou *et al.* synthesized Pt nanoparticles of different sizes (3 nm, 5 nm, and 10 nm).[108] Pt nanoparticles smaller than 3 nm were uniformly encapsulated in UiO-66; however, as particle size increased, the encapsulation efficiency decreased. This effect can be explained by surface energy considerations, consistent with the discussion in Section 2.2.1.

2.2.3. Impact of surface charge. Surface charge on nanoparticle surfaces also influences the NP@OF structure. Long *et al.* demonstrated that MOFs can be uniformly decorated over Pt/CeO_2 NPs by modifying them with sodium polystyrene sulfonate (PSS) under microwave assistance. Modification with PSS altered the zeta potential from +19.3 mV to −16.2 mV, thereby facilitating electrostatic attraction between NP surfaces

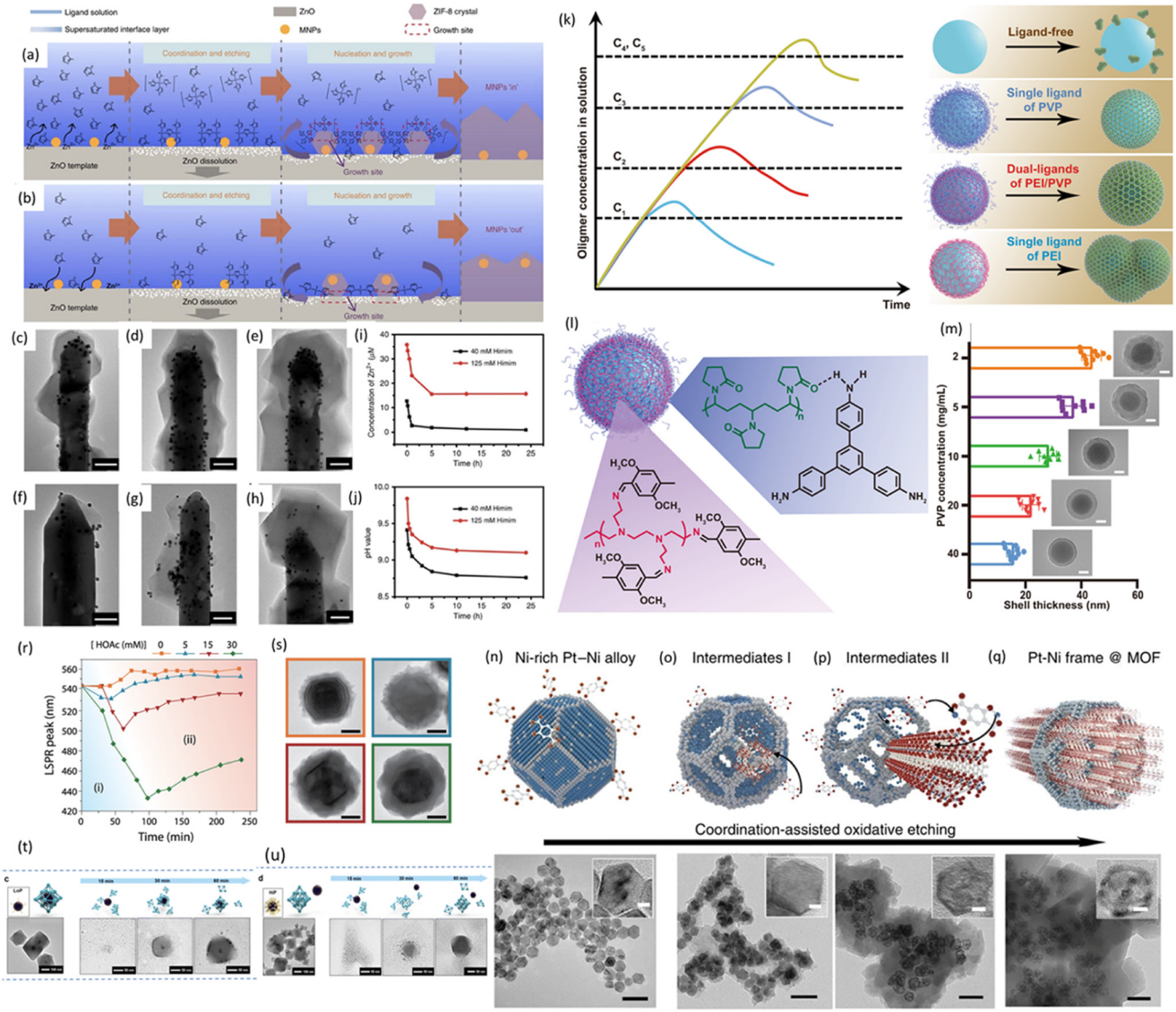

Fig. 5 (a and b) Illustration of two mechanisms for the position-regulated encapsulation of MNPs into ZIF-8. (c–h) TEM images of the product synthesized at high Hmim concentration for various reaction times of (c) 0.5 h, (d) 1 h and (e) 5 h and with low Hmim concentration at the reaction times of (f) 0.5 h, (g) 1 h and (h) 5 h. (i) Concentration of Zn^{2+} *versus* reaction time and (j) pH *versus* reaction time of the ZnO@Au@ZIF-8 at low (black line) and high (red line) concentration of Hmim, respectively. Scale bar: 100 nm. (Variation with pH needs to be explained.) Adapted from ref. 109, with permission from Nature, copyright 2017. (k) Oligomer evolution during COF shell formation on ligand-modified (PVP, PEI, PVP + PEI) and unmodified SiO_2 nanoparticles, based on the LaMer model. C_1–C_3 indicate critical heterogeneous nucleation concentrations on PEI-, PVP + PEI-, and PVP-modified SiO_2, respectively, while C_4 and C_5 denote critical concentrations for homogeneous and heterogeneous nucleation on unmodified SiO_2. (l) Schematic diagram showing the interaction between the dual ligands and monomers. (m) Correlation between the PVP concentration and the thickness of the COF shell in SiO_2@COF core–shell nanoparticles synthesized using the dual-ligand-assisted method. Scale bars: 50 nm. Adapted from ref. 111, with permission from Nature, copyright 2021. (n–q) Schematic and TEM images of the coordination-assisted oxidative etching process. (n) Initial solid Pt–Ni polyhedral. (o) Pt–Ni frame@MOF intermediates I. (p) Pt–Ni frame@MOF intermediates II. (q) Final Pt–Ni frame@MOF. Scale bars: 50 nm (insets are the magnified TEM images. Scale bars: 5 nm).[117] Adapted from ref. 117, with permission from Nature, copyright 2015. (r) Tracking the localized surface plasmon resonance (LSPR) shift of the aluminum (Al) core over time during the growth of the MIL-53(Al) MOF shell, performed with varying initial concentrations of acetic acid (HOAc) in the reaction mixture. The extent of the LSPR shift is categorized into regions (i) and (ii), corresponding to the dissolution and shell growth phases, respectively. (s) Representative TEM images of Al NC@MOF heterostructures synthesized without acetic acid (orange) and with 5 mM (blue), 15 mM (red), and 30 mM (green) acetic acid. Increasing the HOAc concentration in the starting mixture progressively enhances the dissolution rate of the oxide layer, resulting in more pronounced shrinkage of the Al core and the formation of a thicker, denser MOF shell. Adapted from ref. 115, with permission from American Association for the Advancement of Science, copyright 2019. (t) TEM images of LoP@UiO-66 and time-dependent studies of the synthesis of LoP@UiO-66. (u) TEM images of HiP/UiO-66 and time-dependent studies of the synthesis stages of HiP/UiO-66. A high concentration of capping agents on Pt NPs leads to a decrease in the surface energy. Adapted from ref. 108, with permission from Chemical Science, copyright 2023.

Table 3 Summary of reported post-synthetic approaches for synthesizing framework-encapsulated nanostructures

Nanostructure	OF	Resultant structure	Importance	Ref.
PVP stabilized Pt NPs	UiO-66 (MOF)	Pt@UiO-66 core–shell	Surface energy mediated encapsulation	108
PVP stabilized Au nanorods/Au@Pt nanorods/Au@Pt nanotubes	ZIF-67 and ZIF-8	Multiple Au nanorods inside ZIF Au@Pt nanorods inside ZIF Au@Pt nanotubes inside ZIF	• Multicore NRs@OF can be synthesized • The size of OFs can be controlled by controlling ligands	118
Thiolated poly(ethylene glycol) stabilized Au nanorods	NU-901	Au NRs @NU-901 and Au NRs @NU-1000	• Interaction between thiolated PEG and MOF precursor promotes encapsulation • Increase in concentration of Au nanorods decreases the size of the crystallite	114
Pt and Pd nanoparticles	MOFs (nano-UiO-66, nano-UiO-66-NH2, nano- MOF-801)	Pt@nano-MOFs Pd@nano-MOFs	• Nucleation rate of MOFs on the nanoparticles can be controlled by the addition of modulators • Slow nucleation of MOF on the nanoparticles leads to NP@nano-MOF formation	113
Ag@h-SiO_2 nanostructure	COF	Ultrathin COF layer on the surface of Ag nanostructures	• Surface of Ag nanocrystals helps in the oxidation of alcohol to aldehyde upon irradiation of light • The formation process is specific to light	4
ZnO NRs@Au NPs	ZIF-8	ZnO NRs@Au@ZIF-8 composites with Au NPs at different locations	• At high concentration of ligand, dissolution–precipitation mechanism occurs • At low concentrations of ligands, a localized conversion mechanism occurs	109
SiO_2 NP, upconversion NPs, semiconductor NPs	COF	NPs@COF	• Bowl-shaped, yolk@shell, core@satellites@shell nanostructures of several NP@COFs can also be fabricated using dual-ligand strategy	111
TiO_2 hollow nanosphere	ZIF-8	Double-shell TiO_2@ZIF-8	• A double-shell TiO_2@ZIF-8 structure is successfully obtained *via* carboxylation and sonocrystallization process	107
PVP-stabilized Au@AgPt nanorattles	ZIF-8	Au@AgPt encapsulated within ZIF-8	• PVP plays an important role in the encapsulation process	119
Au_{55} clusters	Hexaporphyrin cages	Au_{55}	• Small substrates can enter the caged cluster through the apertures because there is an interstitial gap between the core and the porphyrin shell	120
Pt/CeO_2 NPs	UiO-66-NH_2	Pt/CeO_2@UiO-66-NH_2	• Coating of Pt/CeO_2 with polystyrene sulfonate facilitates electrostatic interaction • Use of microwave leads to uniform growth of MOFs on the surfaces of NPs	121
CdS NRs	Cu-TCPP	Core–shell CdS@Cu-TCPP NRs	• With CdS NRs, Cu-TCPP has a sheetlike structure, but when grown on CdS NRs, Cu-TCPP forms around the NRs	122
Pt NPs	Porphyrinic MOF (PCN-224-RT)	Pt@PCN-222-RT	• A facile stirring method at RT • To obtain Pt@PCN-222 within 24 hours	123

and MOF precursors. Microwave treatment further promoted uniform MOF nucleation on NP surfaces.

In a related strategy, synthesis was initiated by solution-phase binding of metal ions using poly(amidoamine) (PAMAM) dendrimers. The positively charged dendrimers were incorporated into the negatively charged pores of Zr-based MOFs (NU-1000). The extent of electrostatic interactions, and hence NP size and distribution, could be tuned by adjusting the solution pH.

2.2.4. Addition speed of the precursor. Osterrieth *et al.* showed that not only ligand concentration but also the rate of ligand addition controls MOF morphology during NP encapsulation.[114] Specifically, Au nanorod (Au NR)-encapsulated Zr-based MOFs (NU-901) were obtained by adding a DMF solution of H_4TBAPy linker into Zr cluster-modified Au NRs dispersed in DMF and acetic acid. It was observed that rapid injection of these linkers led to the formation of elongated NU-1000 (at low concentration), while slow addition produced prolate-shaped NU-901 MOFs. NU-1000 was favored particularly at low H_4TBAPy/AcOH ratios.

In addition to ligand addition rate, the availability of metal precursors also plays a critical role in nanoparticle growth. H. Robatjazi *et al.* showed that in post-synthetic approaches, the availability of metal precursors can be modulated by adjusting reaction conditions, which in turn influences nanoparticle growth.[115] For example, Al nanoparticles were converted into Al@MIL-53 by the addition of 1,4-benzenedicarboxylic acid (H_2BDC) ligands. As no external source of Al precursor was supplied, it was proposed that Al^{3+} ions present in the surface aluminium oxide layer were dissolved and react with H_2BDC to produce MIL-53 around Al cores. This transformation follows a dissolution-growth mechanism. Evidence was provided by the increase in MOF shell thickness with rising pH (controlled by adding acetic acid). At higher pH, the rate of Al dissolution increased, while MIL-53 nucleation was suppressed due to reduced linker deprotonation. As the

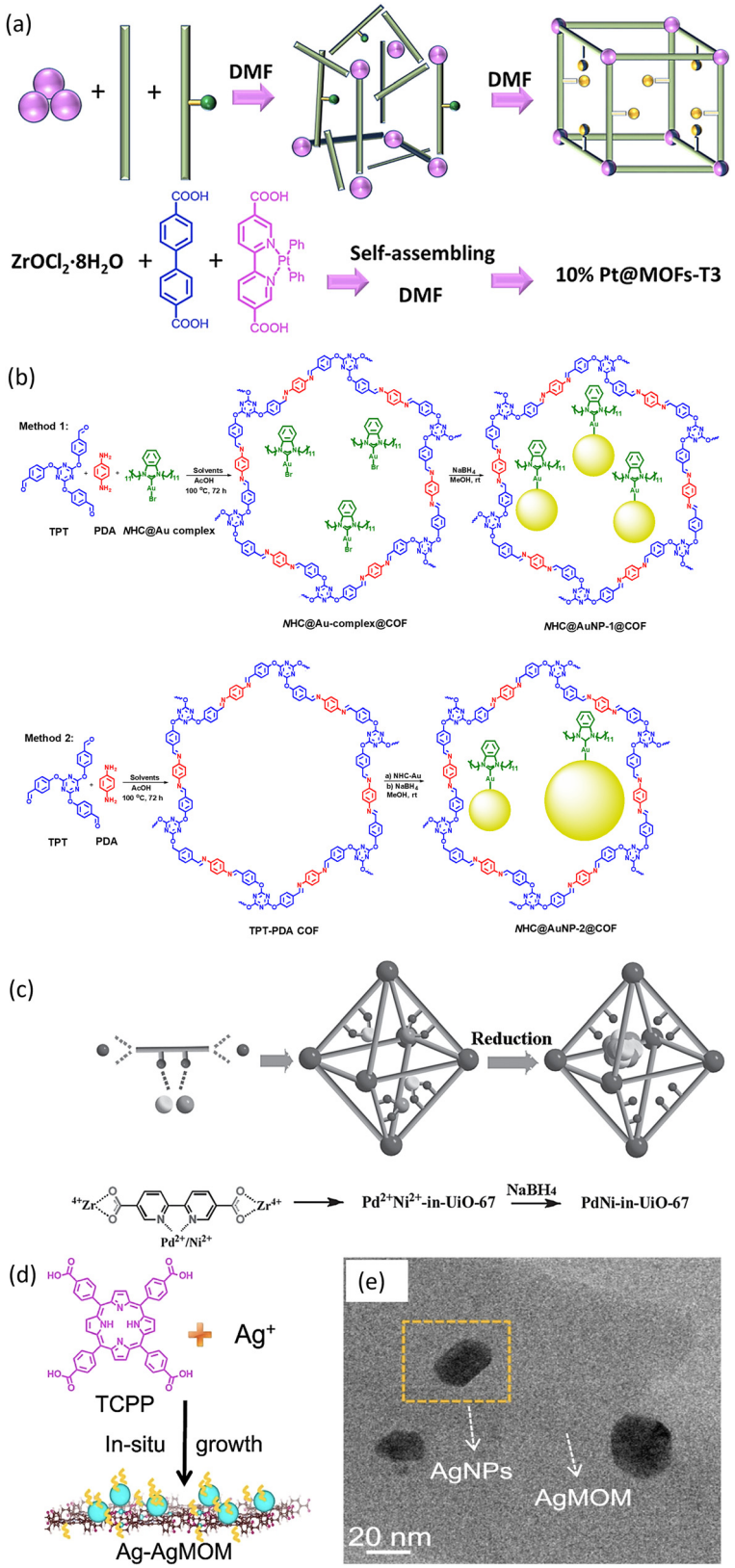

Fig. 6 (a) Schematic illustration of *in situ* one-step synthesis of Pt@MOFs-T3. Adapted from ref. 125, with permission from the American Chemical Society, copyright 2020. (b) Preparation of Au NPs@COF with two different methods. Adapted from ref. 126, with permission from the American Chemical Society, copyright 2024. (c) Schematic representation of the incorporation of PdNi NPs in UiO-67. The assembly of MOFs and the incorporation of metal precursors are performed in a single step. Adapted from ref. 127, with permission from Wiley, copyright 2015. (d) Diagrammatic representation of the Ag–AgMOM one-step *in situ* solvothermal synthesis. (e) Enlarged TEM images of Ag–AgMOM; the lattice of AgMOM was observed. Adapted from ref. 128, with permission from *Nature*, copyright 2023.

reaction proceeded, the solution's pH gradually rose, increasing the concentration of deprotonated linkers, which then initiated MOF growth and simultaneously inhibited further dissolution of the Al nanoparticle core.

The dissolution-growth process was monitored using the sensitivity of the localized surface plasmon resonance (LSPR) of Al@MIL-53, which depends on the size of the Al core and the refractive index of the surrounding medium. Time-dependent changes in LSPR spectra, along with TEM images for different acid concentrations, are shown in Fig. 5r. The analysis revealed two distinct stages. The blue region (region I) indicated that the reaction was dominated by Al dissolution, while in region II, MOF growth became the dominant process. As shown in Fig. 5s, the magnitude of the LSPR blue shift (region I) increased with higher acid concentrations, indicating greater dissolution of Al ions. This, in turn, facilitated the subsequent growth of the surrounding MIL-53 layer.

2.2.5. Concentration of metal nanoparticles. Xu *et al.* showed the construction of Pt-rich Pt–Ni nanoflower@Ni-MOF 74 from Pt–Ni rhombic dodecahedral (RD) structures.[116] For the conversion process, first, oleylamine ligands present on the Pt–Ni RD structure were replaced with CTAB to improve dispersibility with DMF. Subsequently, treatment of CTAB-capped Pt–Ni RD structure with acetic acid led to oxidation of Ni, and the resulting Ni^{2+} ions were captured by 2,5-dihydroxyterephthalic acid (DOT) to form Ni-MOF-74 (Table 3).

2.3. One-pot synthesis

The "one-pot" approach refers to directly mixing precursors of nanostructures with precursors of frameworks. This direct combination leads to the formation of NP@framework structures *via* a self-assembly process. It is a simple and efficient strategy, yet still relatively unexplored for preparing

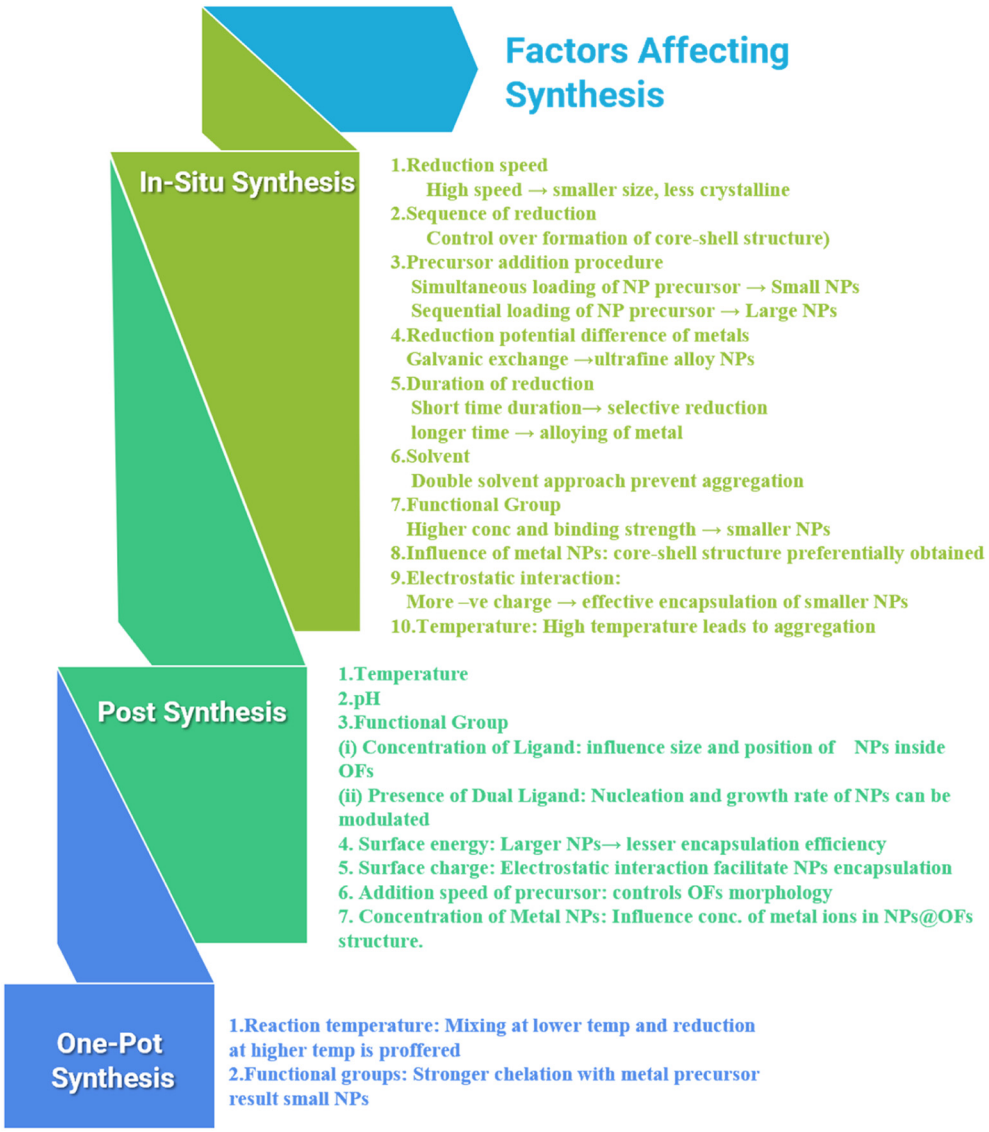

Scheme 2 Impact of different factors on the NP@organic frameworks system obtained using different synthesis strategies

nanostructures. Additionally, using this approach, the diffusion resistance between the outer and the inner surfaces of the frameworks can be efficiently avoided.

In one of the earlier studies, Li *et al.* demonstrated the encapsulation of Pd NPs within UiO-67 MOF functionalized with platinum bipyridine coordination complexes by using a one-pot strategy.[124] Similarly, Wang *et al.* developed a capping and reducing-agent-free strategy to obtain Pt@MOF-s-T3.[125] The synthesis procedure is shown in Fig. 6a. In this case, uniform and well-dispersed Pt NPs formed inside the cavities of MOFs, attributed to the strong complexation of Pt ions with dipyridyl groups and the stabilization provided by dipyridyl ligands.

The advantage of the one-pot approach over conventional *in situ* synthesis was further highlighted by Gamraoui *et al.*, who achieved the encapsulation of ultra-small Au NPs inside a COF.[126] They used N-heterocyclic carbene (NHC)-functionalized Au(I) complexes as Au NP precursors. When these NHC–Au(I) complexes were added during COF precursor assembly, they became incorporated inside the framework pores. Reduction of these NHC–Au(I)@COFs with $NaBH_4$ led to the formation of ultra-small Au NPs inside the COF. However, addition of NHC–Au(I) complexes to preformed COF, followed by reduction, led to the formation of bigger-sized agglomerated Au NPs, as shown in Fig. 6b. This comparison clearly shows the efficiency of the one-pot method.

Reaction temperature also plays a decisive role in one-pot synthesis. Chen *et al.* demonstrated that by carefully controlling the reaction temperature, Pd nanoparticles could be encapsulated inside UiO-67 without the addition of any external reducing agent.[103] Mixing $PdCl_2(CH_3CN)_2$ with a solution of MOF precursors, *i.e.*, $ZrCl_2$ and 2,2′-bipyridine-5,5′-dicarboxylate (H_2bpydc), in DMF at 80 °C led to the incorporation of Pd ions in UiO-67 crystals. The chelating ability of nitrogen atoms in the bipyridyl groups facilitated the incorporation of Pd ions into the UiO-67 crystals. Pd ions present in the UiO-67 framework were reduced by the solvent molecules at high temperature (130 °C). The formed nanoparticles are stabilized by the bipyridyl groups.

This strategy can also be extended to fabricate bimetallic NP@framework structures. For instance, ultrafine Pd, Ni, and PdNi alloy NPs were synthesized inside pores of MOFs using the same approach, as shown in Fig. 6c.[127] Beyond MOFs, Liu *et al.* reported the creation of Ag–AgMOMs, hybrid structures consisting of Ag NPs and an Ag-porphyrin metal–organic matrix (MOM), in a single step, as shown in Fig. 6d. The *in situ* growth enabled by one-pot synthesis allowed silver atoms to be shared at the interface, thereby facilitating efficient electron transmission between Ag NPs and AgMOM (Fig. 6e).[128]

Finally, microwave irradiation significantly reduces the time needed for the one-pot synthesis process. Zhang *et al.* showed that Au NPs could be immobilized within MOD-199 within 2 min using microwave irradiation, achieving Au loadings as high as 5.13%.[129]

The above discussion demonstrates that various factors influence each synthesis procedure in distinct ways. These factors and their corresponding impacts are summarized in Scheme 2.

3. Nanoparticle encapsulation and enhanced stability of the hybrid structures

The encapsulation of nanoparticles within organic frameworks significantly enhances the thermal and chemical stability of both nanoparticles and the host frameworks. This enhancement of stability is primarily due to synergistic electronic interactions between the NPs and the functional groups of the framework as well as from the vibrational restrictions. The structural rigidity and appropriate interactions of metal with the organic counterpart can promote the structural consistency. Ding *et al.* developed Pd–Au nanoparticles supported on a diamine-functionalized UiO-66 framework, which exhibited marked resistance to aggregation and could be recycled seven times during formic acid dehydrogenation.[94] High stability was correlated to the enhanced density of $-NH_2$ groups in MOFs, thereby effectively stabilizing ultra-small PdAu NPs. Similarly, in the case of amine functionality, improved stability was obtained in Pd NPs when combined with Cr-MIL-101.[130]

Muhamed *et al.* showed that the strong binding affinity of Ag and the thiol group can be used to synthesise Ag NP-modified NU-1000. In this process, the NU-1000 MOF was successfully functionalized with –SH groups using the solvent-assisted ligand incorporation method. These –SH groups chelate with Ag(I) ions while simultaneously causing their reduction, resulting in the formation of Ag NPs/NU-1000 nanohybrids.[131] Hamoud *et al.* found that the ligand-driven *in situ* reconstruction of the UiO-66-$(COOH)_2$-Cu hybrid structure provides additional stability to UiO-66-$(COOH)_2$-Cu and enhances its catalytic efficiency. Under solar radiation, the UiO-66-$(COOH)_2$-Cu structure transforms to an anhydride analogue structure UiO-66-$(COO)_2$-Cu. This intra-framework cross-linking *via* anhydride linkage provides additional stability to the framework structures.[132] Zhang *et al.* reported the synthesis of a unique porous organic polymer (POP) containing thiazolo[5,4-*d*] thiazole units, namely TzPOP. The resulting TzPOP–OH has three –OH groups as binding sites in addition to N and S atoms. However, the N and S binding sites can be easily protonated under highly acidic conditions. Nevertheless, the –OH binding sites can effectively bind to Pd(II) ions in a strong acid environment. The importance of strong binding between nanoparticles and the binding groups of the organic frameworks in stabilisation of the overall system has thus been emphasised in the above-mentioned studies.

The incorporation of nanoparticles in the framework structure also limits the vibrational flexibility of the framework structure. In this regard, Wang *et al.* synthesised Au_{25}@M-MOFs (M = Mg, Co, Zn, Ni) by nucleating MOFs on the surface of $Au_{25}(Cys)_{18}$ nanoclusters.[133] The Au_{25}@M-MOF exhibits enhanced photoluminescence (PL) intensity compared to $Au_{25}(Cys)_{18}$, upon excitation at 420 nm. This observation is

attributed to coordination between the metal oxo chain of MOFs and the free carbonyl groups of Cys of Au nanoclusters. This imposes constraints on the vibrations and rotations of Cys ligands, leading to an increase in PL intensity. In addition to the above-mentioned factors, when frameworks are grown on the surface of NPs, a uniform, defect-controlled coating of OFs over the NP surface is observed, due to which the structure becomes more stable.

4. Factors that regulate catalytic activities

The effectiveness of metal nanoparticles in catalytic processes is influenced by several factors, such as size, morphology, surface roughness, presence of defects, surface protective agents, and the nature of the exposed crystal facets. Certain metal NPs, such as Ag, Au, and Cu, possess excellent light absorption capabilities due to their surface plasmon resonance (SPR), which significantly influences the photocatalysis process. Frameworks themselves also serve as excellent catalysts, with their performance depending on structure, dimensionality, types of metal centers, and organic linkers. Importantly, heterostructures comprising both metal NPs and frameworks do not behave solely as a function of either component. Their integration changes the intrinsic properties of both the NPs and the frameworks. Below, key factors influencing the catalytic efficiency of NP@framework structures are outlined.

(i) Structure of the organic framework

The structural characteristics of frameworks strongly influence the catalytic activity of the catalyst. Wang *et al.* reported that Pt@ZIF-7, having varying sizes of ZIF-7, could be synthesized by controlling the nucleation and growth rate of ZIF on preformed Pt NPs.[113] These Pt@nano-ZIF structures effectively catalyzed the hydrogenation of *n*-hexene. Pt@nano-ZIF, having 40 nm ZIF, exhibited better conversion efficiency than those with 850 nm and 1.5 μm ZIF. This is attributed to the shorter diffusion path from the MOF surface to the active sites.

Strain in the frameworks also influences the catalytic activity of NP@frameworks. The incorporation of NPs can induce strain, which modifies the catalytic activity of NP@framework systems. For instance, in the *in situ* synthesis, excessive loading of metal precursors may deform frameworks with small pores, and reaction conditions may further accelerate framework degradation. Nevertheless, these quasi-NP@quasi-framework structures often develop strong interactions between NPs and frameworks. Tsumori *et al.* prepared an Au/MIL-101 structure *via* a controlled deligandation process. These Au NP-quasi-MIL-101 structures have stronger interactions between Au NPs and

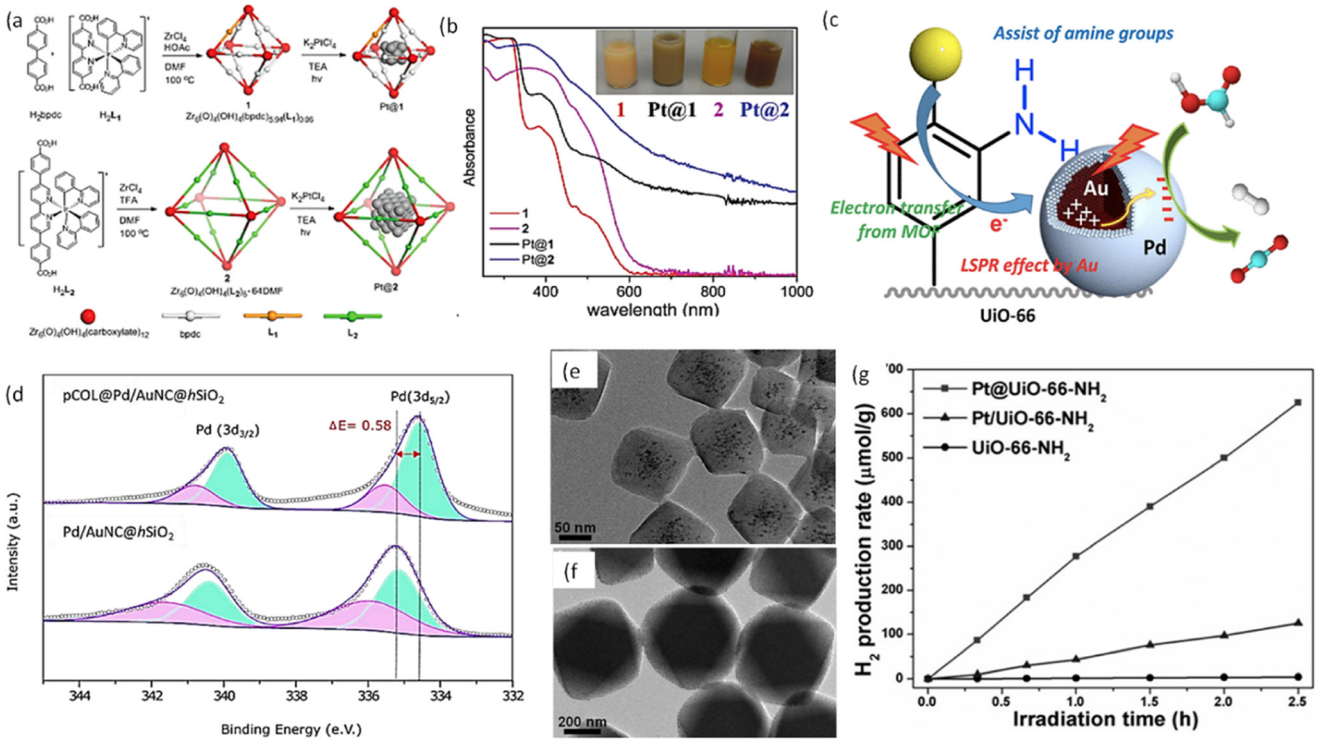

Fig. 7 (a) Synthesis procedure of Zr-carboxylate MOFs (**1** and **2**) followed by photoreduction of K_2PtCl_4 for Pt NP loading within the MOF cavities to form Pt@**1** and Pt@**2** structures. (b) Diffuse reflectance spectra of **1** (red), Pt@**1** (black), **2** (purple), and Pt@**2** (blue). A photograph of suspensions of these samples is shown in the inset. Adapted from ref. 136, with permission from the American Chemical Society, copyright 2012. (c) Synergetic influence of SPR of Ag NPs and $-NH_2$ group in dehydrogenation of HCOOH. Adapted from ref. 143, with permission from the American Chemical Society, copyright 2017. (d) Comparative XPS spectra of Pd (3d) in pCOL-Pd/AuNC@h-SiO_2 and Pd/AuNC@h-SiO_2. Adapted from ref. 4, with permission from Nature, copyright 2023. (e and f) Typical TEM images of (e) Pt@UiO-66-NH_2 and (f) Pt/UiO-66-NH_2. (g) Photocatalytic hydrogen-production rates of UiO-66-NH_2, Pt@UiO-66-NH_2, and Pt/UiO-66-NH_2. Adapted from ref. 145, with permission from Wiley, copyright 2016.

Cr–O metal nodes. These interactions activated Cr–O sites for O_2 uptake and activation, thereby enhancing CO oxidation.[134] Similarly, Yang *et al.* highlighted that strain induced during NP incorporation impacts electrocatalytic efficiency. Using the vapor-phase infiltration (VPI) method, they introduced Zn coordination sites into MOFs. Prolonged VPI treatment converted these sites into ZnO NPs, introducing strain in the system.[135] This strain enhanced the electrocatalytic reduction efficiency and selectivity of the MOF.

(ii) Size of the nanoparticles

The size of NPs directly influences their surface area, electronic structure, and thus catalytic activity. Wang *et al.* revealed that by modulating the ligand, the pore size of the frameworks could be adjusted, which in turn controlled NP size, as shown in Fig. 7a. They further reported that the size of Pt NPs influenced the efficiencies of the photocatalytic hydrogen evolution reaction (HER).[136] Specifically, Pt@MOF structures having 5–6 nm Pt NPs were shown to have better catalytic activity than Pt@MOF structures having 2–3 nm Pt NPs. The enhanced catalytic efficiency was attributed to higher light absorbance (Fig. 7b) and more efficient electron transfer from $[Ir^{3+}(ppy)_2(bpy^{\bullet-})]$ species to Pt NPs. A contradiction was observed by Mian *et al.*[137] They found that Cu NPs having ~1.5 nm placed in NU-907 exhibited better catalytic activity than ~0.9 nm sized Cu NPs placed in NU-901 for the selective hydrogenation of acetylene to ethylene. Theoretical calculations explained this behavior: smaller, highly curved particles required higher activation energy for the reaction compared to larger, flatter surfaces, thereby reducing catalytic efficiency.

(iii) Plasmonic effect of nanoparticles

Certain NPs, such as Ag, Au, and Cu, strongly absorb solar electromagnetic radiation because of the collective oscillation of free electrons upon interaction with light. This phenomenon is known as surface plasmon resonance (SPR).[138,139] Integration of plasmonic NPs with frameworks enhances their applicability.[140,141] For instance, Qin *et al.* reported that plasmonic Au NPs@MIL-100(Fe) displayed improved photocatalytic performance for the oxidation of benzyl alcohol when illuminated under visible light.[142] This improved photocatalytic performance was attributed to the migration of SPR-excited hot electrons from plasmonic Au NPs to MIL-100(Fe), which facilitated the generation of more active $O_2^{\bullet-}$ radicals.

SPR can also help in the activation of non-plasmonic catalysts. Wen *et al.* presented a unique core–shell ZIF-8@Pd_2-Ag_1@ZIF-67, which acted as an excellent catalyst for photocatalytic selective dehydrogenation of formic acid (HCOOH).[143] Here, the catalytic activity originated from Pd sites electronically promoted under visible light due to the Ag plasmon resonance, combined with the favorable core–shell MOF architecture, as shown in Fig. 7c. In another example, Wen *et al.* established that plasmonic Au@Pd nanoparticles supported on titanium-doped, amine-functionalized zirconium-based MOFs (UiO-66($Zr_{100-x}Ti_x$)) exhibited synergistic activity, significantly enhancing room-temperature hydrogen production through the photocatalytic dehydrogenation of formic acid.[71] Among the tested catalysts, Au@Pd-UiO-66($Zr_{85}Ti_{15}$) outperformed both Au-UiO-66($Zr_{85}Ti_{15}$) and Pd-UiO-66($Zr_{85}Ti_{15}$). This superior activity was attributed to the generation of electron-rich Pd sites through electron transfer from Au NPs to Pd. Since formic acid is electron-deficient, it preferentially adsorbs on Pd, thereby facilitating the electron transfer and catalysis.

(iv) Change in electronic environment

Integration of NPs with frameworks also modifies the electronic charge distribution of both components, with

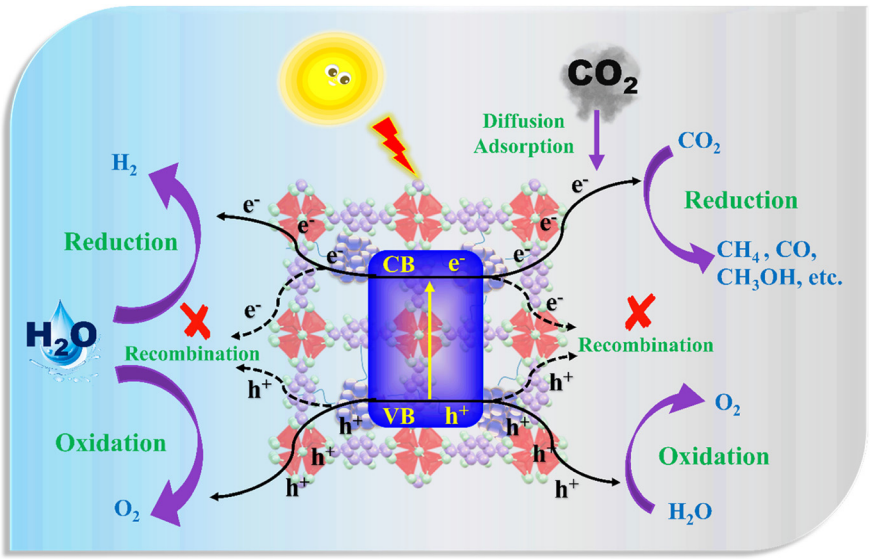

Scheme 3 Proposed mechanism of photocatalytic CO_2 reduction process and H_2 production from water splitting.

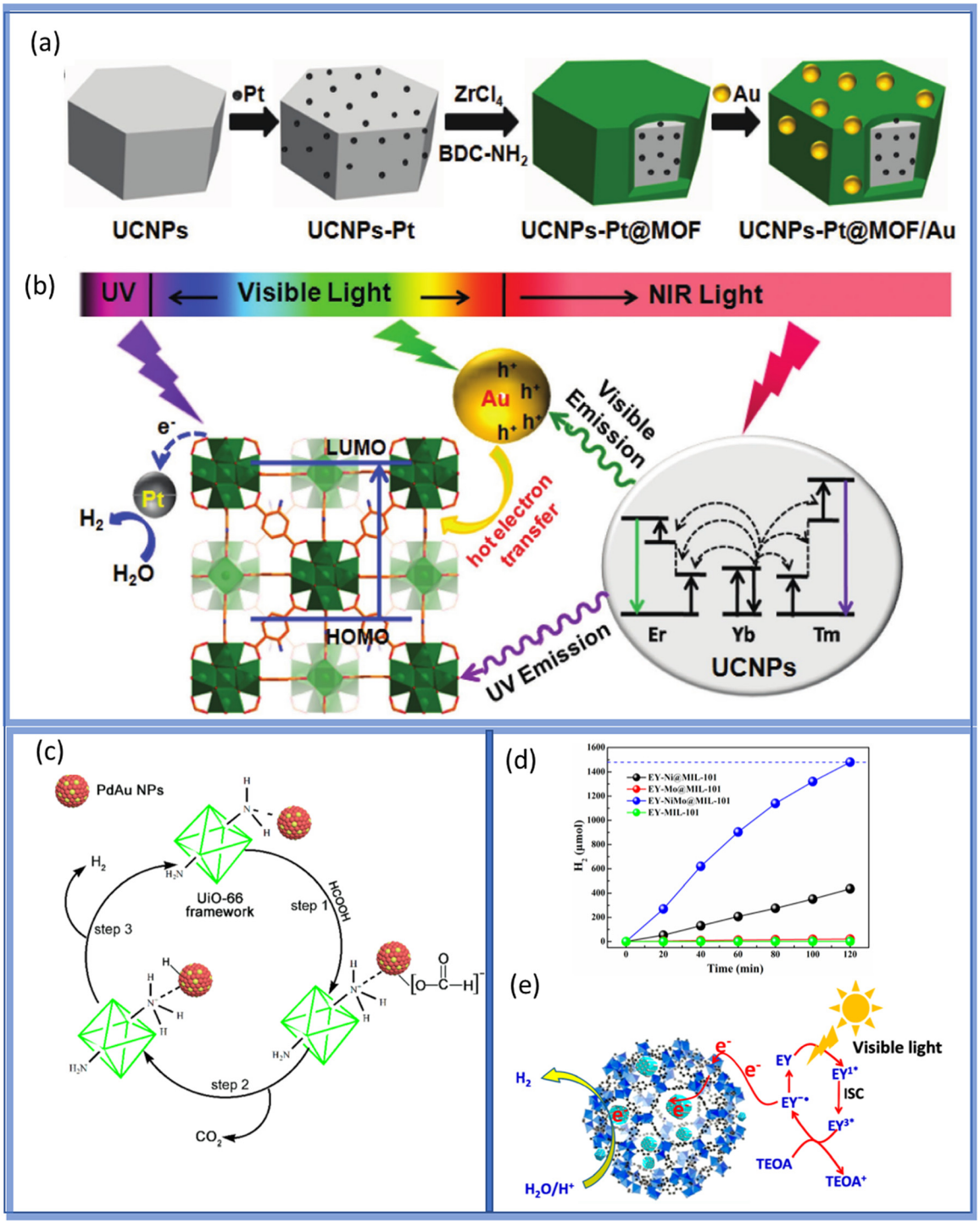

Fig. 8 (a) Schematic of the synthetic process for UCNPs-Pt@MOF/Au. (b) Mechanism involved in photocatalytic H_2 production. Adapted from ref. 122, with permission from the American Chemical Society, copyright 2024. (c) Mechanism for H_2 generation from FA over the $Pd_{0.8}Au_{0.2}$/UiO-66-$(NH_2)_2$ catalyst. Adapted from ref. 94, with permission from the American Chemical Society, copyright 2021. (d) Hydrogen evolution profiles of EY–MIL-101, EY–Ni@MIL-101, EY–Mo@MIL-101, and EY–NiMo@MIL-101 photocatalysts over time. Adapted from ref. 146, with permission from the American Chemical Society, copyright 2016. (e) Mechanism of the hydrogen evolution reaction (HER) over eosin Y-sensitized NiMo@MIL-101 under visible light irradiation. Adapted from ref. 146, with permission from the American Chemical Society, copyright 2016.

electron transfer occurring either from NP to framework or *vice versa*. Acharya *et al.* confirmed that coating of Pd/Au NPs with a thin layer of COFs altered the electronic state of both NPs and frameworks. Density functional theory (DFT)-based Bader charge analysis and XPS measurements provided evidence that coating Pd NPs with a thin layer of COFs made them more electron-rich, as shown in Fig. 7d.[4] Similarly, Shen *et al.* unveiled the role of metal–O clusters in regulating

the electronic environment of composite catalysts.[144] Fe–O cluster-based MOFs decreased the electron density of encapsulated Pt nanoparticles, thereby suppressing the complete hydrogenation of phenylacetylene and enabling the selective semi-hydrogenation of phenylacetylene to styrene with ~80% selectivity. Conversely, MOFs containing Cu–O clusters promoted the formation of highly oxidized Pt NPs and released Cu^{2+} ions, which jointly contributed to the complete deactivation of Pt NPs during hydrogenation.

(v) Position of nanoparticles inside the MOF

The spatial location of NPs within frameworks critically affects catalytic behaviour. Xiao *et al.* synthesized Pt NPs inside UiO-66-NH_2, termed as Pt@UiO-66-NH_2, and compared them to Pt NPs outside the framework, as illustrated in Fig. 7e and f.[145] Pt@UiO-66-NH_2 showed superior H_2 production efficiency because the shorter electron transfer pathway facilitated faster charge migration, as shown in Fig. 7g. Consistently, other studies have highlighted that NPs positioned near framework surfaces often exhibit higher catalytic activity than those deeply confined within the MOF matrix.[109]

Beyond these key factors, catalytic efficiency is also influenced by structural changes during catalysis, reaction conditions, and the concentration of NPs within frameworks. Each of these parameters can alter stability, accessibility of active sites, and overall catalytic performance.

5. Photocatalytic applications

Integrating nanostructures with frameworks offers several key advantages: (i) the formation of a Schottky junction, which enhances charge separation and transfer; (ii) localized surface plasmon resonance (LSPR), which broadens the light absorption range and facilitates the excitation of active charge carriers; and (iii) suppression of nanoparticle aggregation.

The overall photocatalytic activity can be described through the following schematic diagram (Scheme 3). Electron–hole pairs are generated when NP@OFs are illuminated with light. The electrons are used for the reduction process, leading to the formation of H_2 from water and value-added chemicals from CO_2. Similarly, the oxidation process leads to the formation of oxygen. To have maximum photocatalytic efficiency, electron–hole recombination should be avoided.

H_2 production

Given the global green demand for green and sustainable energy, photocatalytic hydrogen evolution reactions (HERs) have gained significant attention. Semiconductor NPs are often used as catalysts for photocatalytic HER. Shi *et al.* reported that the photocatalytic activity of CdS was greatly enhanced when incorporated within a porphyrin framework (4,4′,4″,4‴-porphine-5,10,15,20-tetrayl)tetrakis(benzoic acid) (TCPP).[122] They prepared CdS@Cu-TCPP-Pt nanorod catalysts with an H_2 production rate of 20.75 mmol g^{-1} h^{-1}. The superior photocatalytic performance was attributed to a favorable energy-level alignment of CdS and Cu-TCPP and their interfacial interaction, which promoted efficient separation of photogenerated carriers.

Similarly, Li *et al.* have constructed a core–shell Pt NPs–upconversion NPs@MOF/Au structure, which can absorb a broad spectrum of solar light, as shown in Fig. 8a. In this system, UV light excites the MOF, transferring electrons to Pt, which acts as the active site for hydrogen production. Meanwhile, the SPR effect of Au enhances absorption of visible light, generating hot electrons that transfer first to the LUMO of the MOF and then to Pt NPs. Under NIR irradiation, the energy transfer from Yb^{3+} causes excitation of Tm^{3+} and Er^{3+} ions in UCNPs. The MOF absorbs the upconverted UV emission from Tm^{3+}, generating electron–hole pairs whose electrons migrate to Pt for hydrogen production. Concurrently, the upconverted green emission from Er^{3+} couples with Au SPR, producing hot electrons that further transfer into the MOF, as shown in Fig. 8b. These dual charge-transfer pathways synergistically improve NIR harvesting and overall photocatalytic activity.

Shi *et al.* further highlighted that integrating Cu-TCPP with CdS nanorods (NRs) expanded the light absorption range of CdS but also reduced the rate of recombination of electron–hole pairs.[122] Subsequent incorporation of these structures with Pt NPs further suppressed e–h recombination and hence boosted the rate of H_2 evolution from selective oxidation of benzylamine.

The SPR effect has also been exploited in Ag-based systems. A similar SPR influence on the catalytic efficiency of Ag NP–Ag porphyrin metal–organic matrix (Ag–AgMOM) on the H_2 evolution reaction from water was demonstrated by Liu *et al.*[128] The uniqueness of this structure lies in the shared Ag atoms at the Ag NP/AgMOM interface, which enable efficient interfacial charge transfer. Under visible and full-spectrum light irradiation using a full-spectrum 300 W Xe lamp, the Ag–AgMOM exhibited H_2 production rates of up to 1025 μmol h^{-1} g^{-1} and 3153 μmol h^{-1} g^{-1}, respectively. Additionally, Ag NPs contribute to stabilizing the otherwise unstable Ag node-based porphyrin MOM by sharing Ag atoms while their SPR effect broadens light harvesting. The presence of a small amount of poly(vinylpyrrolidone) (PVP) at the Ag/AgMOM interface permits efficient charge transfer. All these factors collectively make Ag–AgMOM an efficient catalyst.

Furthermore, the functionalities present in the framework compound play an important role in the catalytic activity by facilitating substrate adsorption followed by chemical transformation. Ding *et al.* synthesized a PdAu NP-loaded UiO-66-$(NH_2)_2$ MOF using a double-solvent (H_2O/*n*-hexane) method followed by $NaBH_4$ reduction.[94] The PdAu-loaded UiO-66-$(NH_2)_2$ catalyst exhibited superior formic acid dehydrogenation performance compared to PdAu@UiO-66-NH_2, with enhanced stability over a wide temperature range. This improvement was attributed to the stronger stabilization effect of the diamine-functionalized UiO-66-$(NH_2)_2$ framework, as shown in Fig. 8c.

In general, bimetallic NPs incorporated within frameworks show enhanced activity compared to their single-metal

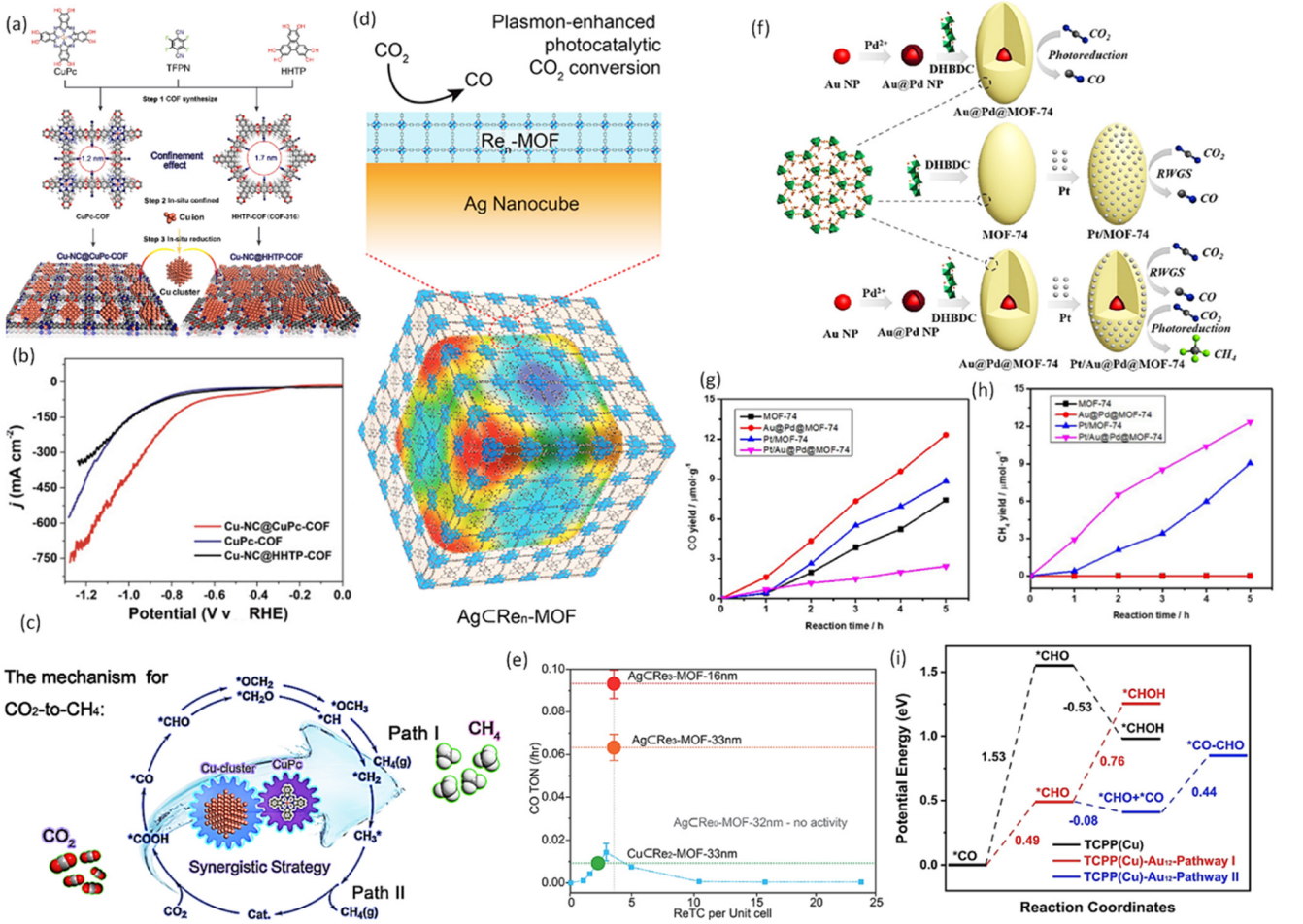

Fig. 9 (a and b) Schematic of the synthesis process of Cu NC@CuPc and Cu NC@HHTP, and the LSV curve showing CO_2-to-CH_4 conversion, respectively. (c) Proposed mechanism for the CO_2 reduction electrochemically. Adapted from ref. 153, with permission from Elsevier, copyright 2023. (d) Re_n-MOF coated on a Ag nanocube for enhanced photocatalytic conversion of CO_2. Adapted from ref. 156, with permission from the American Chemical Society, copyright 2017. (e) Photocatalytic CO_2-to-CO conversion activity of Re_n-MOFs, Ag⊂Re_0-MOF, Cu⊂Re_2-MOF, and Ag⊂Re_3-MOFs with MOF thickness of 16 nm and 33 nm. Adapted from ref. 156, with permission from the American Chemical Society, copyright 2017. (f) The formation energy of key intermediates along with the reaction coordinates for TCPP(Cu) and TCPP(Cu)–Au_{12}. Adapted from ref. 80, with permission from Nature, copyright 2022. (g) Illustration depicting the assembly of Au@Pd@MOF-74, Pt/MOF-74, and Pt/Au@Pd@MOF-74 catalysts, along with their functions. (h) and (i) represent CO and CH_4 yield for MOF-74, Pt/MOF-74, Au@Pd@MOF-74, and Pt/Au@Pd@MOF-74, respectively. Adapted from ref. 157, with permission from Elsevier, copyright 2019.

counterparts. For instance, Wen *et al.* reported that Au@Pd NPs, when integrated with titanium-doped zirconium-based amine-functionalized MOF (UIO-66(Ti_xZr_{100-x})), act as an excellent catalyst for H_2 production from formic acid.[143] Zhen *et al.* revealed that NiMo@MIL-101 outperforms both Mo@MIL-101 and Ni@MIL-101 for H_2 generation.[146] Photocatalytic activity was tested under 420 nm irradiation in triethanolamine (TEOA) and H_2O solution and in the presence of eosin Y (EY), as shown in Fig. 8d.

The mechanism of the H_2 evolution process is depicted in Fig. 8e, where electrons generated by EY are transferred to NiMo sites *via* the highly conductive MIL-101. Hydrogen adsorbed on NiMo is subsequently converted into H_2 molecules. Density functional theory (DFT) calculations further confirmed that the hydrogen adsorption free energy (ΔG_H) of $MoNi_4$–H_{ads} (458 kJ mol^{-1}) was found to be lower than that of Ni–H_{ads} (537 kJ mol^{-1}), which explains the superior catalytic activity of NiMo catalysts.

Beyond bimetallic effects, the light-trapping efficiency of frameworks can also be tuned to boost the photocatalytic performance. Liu *et al.* synthesized a series of donor–acceptor network-type COFs that confine $PtCo_2$ nanoclusters.[147] Under visible light irradiation, these $PtCo_2$@COFs act as an efficient photocatalyst with a turnover frequency (TOF) of 486 min^{-1}. This effect is ascribed to the strong electronic interactions between the COF and $PtCo_2$ nanoclusters. Furthermore, the D–A type COF significantly improves light-trapping capability by adjusting the electron-acceptor units within the framework, while also facilitating the transfer of photogenerated electrons from the D–A type COF to $PtCo_2$ nanoclusters, which aids in the adsorption and activation of H_2O. Additionally, $PtCo_2$@COF demonstrated exceptional stability, attributed to its enhanced

resistance to NC aggregation, a result of the nanopore confinement effect within the D–A type COF that prevents nanocluster aggregation.

CO_2 reduction

Combining frameworks with encapsulated metals, such as metal NPs and NCs, leverages the unique qualities of each component to create a synergistic effect.[21,148] It is worth noting that a series of recent studies have demonstrated that the coexistence of single-site metal active centers and metal nanoclusters in photosensitised MOFs can remarkably activate and convert CO_2 through the direction–orientation charge-transfer mechanism and effective photoluminescence, achieving complex catalytic reactions like CO_2 carbonylation.[21,149] Among them, Cu NPs and NCs are widely recognized as efficient catalysts for CO_2 reduction.[150–152] Confinement of metal nanostructures within frameworks restricts their agglomeration and regulates their electronic and geometric structures, thereby enhancing their catalytic activities.

For example, Zhang *et al.* developed confined Cu nanoclusters within CuPc (2,3,9,10,16,17,23,24-octahydroxyphthalocyaninato copper) and HHTP (2,3,6,7,10,11-hexahydroxytriphenylene) COFs, as shown in Fig. 9a.[153] The linear sweep voltammetry curve in Fig. 9b indicated that the efficiency of the catalyst for the conversion of CO_2 to CH_4 follows the order CuNC@CuPc > CuNC > CuNC@HTTP. In particular, Cu-NC@CuPc-COF achieved a faradaic efficiency of approximately 74 ± 3% (at ~1.0 V *vs.* RHE), along with a peak current density of 538 ± 31 mA cm^{-2} (at ~1.2 V *vs.* RHE). This high efficiency of CuNC@CuPc-COF is attributed to the synergistic effect between Cu NCs and the CuPc-COF. The CO_2-to-CH_4 conversion proceeds *via* two reaction pathways, as illustrated in Fig. 9c. DFT calculations confirmed that the free energy barriers for COOH and CO radical formation are significantly reduced, thereby facilitating the overall conversion. Expanding on Cu-based systems, Kung *et al.* reported a Cu NP-embedded MOF (NU-1000) prepared by solvothermal deposition of Cu^{2+} ions into NU-1000, followed by electrochemical reduction of Cu^{2+} ions.[154] The resulting Cu NPs exhibited promising electrochemical activity for CO_2 reduction. However, the products included CH_4, C_2H_4, and CO with poor selectivity. This limitation was attributed to variations in particle size, degree of agglomeration, and local CO_2 concentration. To improve selectivity, bimetallic interfaces are often utilized. It is well known that metal–semiconductor interfaces such as Cu/ZrO_2 and Cu/ZnO play critical roles in the hydrogenation of CH_3OH from CO_2. However, during the catalysis process, particle growth and structural reorganization significantly reduce the activity of these interfaces. An *et al.* revealed that confinement of Cu/ZnO_x NPs in pre-assembled bpy and $Zr_6(\mu_3\text{-}O)_4(\mu_3\text{-}OH)_4$ sites in UiO-bpy MOFs prevents aggregation of NPs and preserves high activity.[93] Other metal NPs, besides Cu, also influence CO_2 reduction. For instance, H. Robatjazi *et al.* established that Al@MIL-53 can be used as a catalyst for the decomposition of CO_2.[115] Under illumination, CO_2 was selectively converted into CO, driven by the plasmonic effect of Al NPs. Likewise, Chen *et al.* highlighted the influence of Ag NPs on the photoreduction of CO_2.[155] They showed that Ag@Co-ZIF-9 acted as an effective photocatalyst for CO_2-to-CO conversion, with selectivity of the catalyst improving with an increase in Ag content. Similarly, plasmonic Ag nanocube-coated Re_n-MOF (Ag⊂Re_n-MOF) structures acted as photocatalysts for the conversion of CO_2 to CO.[156] The catalytic activity of these structures was attributed to the cooperative effect between spatially confined photoactive Re centers and the intensified near-surface electric fields at the surface of Ag nanocubes, as shown in Fig. 9d. Cooperatively enhanced photocatalytic activity in Re_n-MOFs required a delicate balance of closeness between photoactive centers. In comparison to the Re_3-MOF under visible light, the improved Re_3-MOF on silver nanocubes exhibited a sevenfold increase in CO evolution rate (Fig. 9e). Additionally, compared to molecular H_2ReTC, the Ag⊂Re_3-MOF structure showed long-term stability of up to 48 hours, and after 48 hours, the CO generated from Ag⊂Re_3-MOF was nearly twice that of H_2ReTC. Further, noble metal-incorporated frameworks also showed tunable selectivity. Zirconium-based PCN-222 MOFs containing metalloporphyrin Cu centers with embedded Au nanoneedles acted as efficient catalysts for CO_2 reduction.[80] AuNN@PCN-222(Cu) selectively reduced CO_2 to ethylene, whereas AuNP@PCN-222(Cu) and PCN-222(Cu) primarily produced CO and H_2, respectively. The high ethylene selectivity of AuNN@PCN-222(Cu) was attributed to an energetically favorable path for CO–CHO formation, as illustrated in Fig. 9f.

In addition, Han *et al.* demonstrated that multi-metallic NPs supported on MOF-74 serve as an excellent photocatalyst for CO_2 reduction.[157] They fabricated a Pt/Au@Pd@MOF-74 catalyst by growing MOF-74 on pre-formed Au@Pd NPs and subsequently adding Pt NPs, as shown in Fig. 9g. In photocatalytic conversion of CO_2, Au@Pd@MOF-74 selectively generated CO from CO_2, whereas Pt/Au@Pd@MOF-74 favored CH_4 with 84% selectivity, as seen in Fig. 9h and i. Since CO_2-to-CO conversion is a two-electron process, while CO_2 to CH_4 requires four electrons, Pt's ability to absorb and transfer more electrons explains its effectiveness in promoting CH_4 formation.

Su *et al.* reported that the addition of ZIF-8 precursor to PVP-capped Au@AgPt nanorattles (NRTs) leads to the formation of Au@AgPt@ZIF-8 nanostructures.[119] These nanostructures served as highly efficient catalysts for the conversion of CO_2 to CH_4. Building on structural factors, Yang *et al.* revealed that internal strain within MOFs can enhance their electrocatalytic CO_2 reduction efficiency and selectivity.[135] Specifically, growth of ZnO NPs inside MOFs *via* the VPI method created 2.8% additional internal strain, which improved CO_2 to CO reduction efficiency by a factor of four compared to unstrained MOFs. Semiconductor NP embedded in OFs also acts as an efficient catalyst for CO_2 reduction. Yao *et al.* have shown that $BiVO_4$ nanocluster-embedded MIL act as an excellent catalyst for the CO_2 to urea conversion process in a mixed O_2/air/N_2 atmosphere.[158] Reaction conditions also play a crucial role. CO_2 reduction under acidic conditions improves the carbon utilization rate compared to alkaline conditions. However, under acidic

conditions, the hydrogen evolution reaction (HER) competes strongly with CO_2 reduction. To address this limitation, Wan *et al.* established that conductive 2D NiPc-based MCOF (NiPc-MTAA) frameworks, coupled with metal tetraaza[14]-annulene linkages, act as efficient electrocatalysts for CO_2 reduction in acidic electrolytes. In comparison to 2D NiPc-based MOFs (NiPc-MN_4), these MCOFs demonstrated superior electrical conductivity and stability, attributed to full in-plane π-delocalization.[159] Moreover, the NiTAA node optimized the electron distribution of 3d orbitals by shifting the d-band center closer to the Fermi level, thereby facilitating easier activation of CO_2.

6. Conclusion and outlook

The encapsulation of nanoparticles within porous frameworks, such as MOFs and COFs, has emerged as a rapidly growing and dynamic area of research. These hybrid materials combine the unique physicochemical properties of nanoparticles with the structural tunability, high surface area, and functional versatility of the host frameworks. This synergy opens new possibilities for applications in catalysis, sensing, energy storage, drug delivery, and environmental remediation. In this review, we present a comprehensive overview of the most significant recent advancements in the design, synthesis, and application of NP-encapsulated frameworks, highlighting key strategies, challenges, and future directions in the field. NPs can be grown on pre-formed MOFs (*in situ* approach), or MOFs can be grown on pre-formed NPs (post-synthetic approach). This review provides a critical analysis of the underlying factors that influence the encapsulation process, with emphasis on extended stability and on-demand functionality for catalysis. Importantly, frameworks and NPs do not act as individual entities in NP@framework structures but instead function synergistically. Frameworks restrict NP aggregation, thereby enhancing the stability of NPs, which in turn improves their catalytic performance under harsh conditions. Conversely, NPs also provide stability to organic frameworks by imposing restrictions on their flexibility. In post-synthesis approaches, the nucleation of organic frameworks on nanoparticle surfaces often leads to the formation of defect-controlled, uniform, and stable structures. Both frameworks and NPs mutually influence the electronic environment of each other, which strongly impacts catalytic performance. In addition, other factors such as the size and morphology of NPs, their electronic environment, surface-active agents, framework dimensions, and functional groups also influence catalytic activity. A detailed analysis of the factors is provided in this review. The advantages of these structures, mentioned below, highlight future possibilities that need exploration.

(i) The advantages of NPs@frameworks structures lie in the ability to generate a vast library of materials owing to the diverse availability of both NPs and frameworks. Since significant property changes can be achieved with slight structural modifications, there is a strong potential to expand the existing library. Recent developments in complex heterostructures further broaden this scope. Dimensionality also impacts catalytic efficiency. Yang *et al.* have demonstrated that a reduction in the thickness of 3D MOFs enhances their catalytic efficiency for electrochemical CO_2 reduction.[160] They showed that compared to 3D MOFs, monolayer MOFs with a thickness of 1.8 nm exhibited a higher faradaic efficiency for CO production (93% compared to 51% for 3D MOFs). Crystal engineering of 2D framework nanosheets has been shown to significantly influence photocatalytic performance. Hence, these structures represent promising future catalysts for diverse reactions. Extensive studies are still required to develop new catalyst systems. For instance, yolk–shell and mull architectures, as well as NP incorporation into complex structures such as MOF@MOF, MOF@COF, and MOF/COF composites, warrant further exploration. A recent study by Chu *et al.* showed that control over the internal electric field in MOF/COF heterojunctions can be achieved by engineering crystal facets.[161] Similarly, the influence of the crystal facet of NPs on catalytic processes is well evidenced. However, strategies to control the crystal facets of both NPs and organic frameworks as well as their interfacial connections need to be developed to achieve improved catalytic efficiencies.

(ii) Frameworks can effectively stabilize small-sized NPs. However, since catalytic reactions are often carried out under harsh conditions, frameworks must be designed with improved robustness. In addition, scalable synthesis strategies are essential to enable the commercial-scale production of these materials. A seed-mediated method developed by Han *et al.* operates at lower temperatures and facilitates the production of highly crystalline MOFs, which can be readily scaled up.[162]

(iii) As discussed earlier, frameworks act as transporters of charge carriers during photocatalysis. However, their conductivity depends on several factors, including the functionality of metal centers and bridging ligands, the nature of the framework, and its dimensionality. Therefore, detailed investigations are needed to clarify how these parameters influence integrated NP@framework systems.

(iv) The strong synergic effects between NPs and frameworks are well recognized. However, the extent and precise nature of these interactions as well as their influence on catalytic behavior remain unclear. In-depth mechanistic studies using *in situ* techniques are required to unravel the underlying principles.

(v) These materials often face intrinsic limitations in their structural tunability, which restricts adaptability to evolving application requirements. Such constraints can hinder the optimization of their physicochemical properties, ultimately limiting their overall performance.

(vi) Since the properties of NPs are strongly influenced by their size and shape, further research is required to successfully incorporate NPs with different morphologies into various frameworks. Uniformly distributed NPs show enhanced catalytic efficiencies compared to non-uniformly distributed ones. In this study, we analyse the factors that influence the spatial distribution of NPs inside framework structures. However, further studies are required to fully understand the synergy between these factors.

(vii) Defect engineering plays a critical role in catalysis.[163] For example, Fei *et al.* designed a new type of defect-rich thulium(III) metal–organic framework that acted as a superior CO_2 fixation catalyst.[164] However, the low integration of NPs inside OFs influences the defect of OFs, which is still unexplored and needs research. Photo responsivity and multilevel electron transfer of cluster-included framework material plays a vital role in the enhancement of the lifetime of electrons for photocatalytic applications.

In summary, the lack of precise control over morphology, pore size, surface functionality, and framework flexibility can impede effective interactions with guest molecules or nanoparticles, thereby reducing efficiency in targeted applications. Overcoming these challenges is essential to unlock the full potential of framework-stabilized nanostructures and to develop versatile, high-performing materials tailored to specific technological needs. Considerable research efforts have already demonstrated the remarkable catalytic efficiencies of NP@frameworks across diverse reactions. Nevertheless, extended and focused investigations are required, particularly on synthesis strategies, stability under harsh conditions, mechanistic insights, and semiconductor-based systems, to advance these materials into practical applications. With continued progress, NP@frameworks hold strong promise as the "materials of a sustainable society".

Conflicts of interest

There are no conflicts to declare.

Data availability

No primary research results, software, or code have been included, and no new data were generated or analysed as part of this review.

Acknowledgements

RS gratefully acknowledges the BRNS-funded project (Sanction No. 58/14/04/2025-BRNS) supported by the Department of Atomic Energy (DAE), Government of India. PS acknowledges extra mural research funding under MRIP 2024-Chemistry (24EM/CH/27) from the Department of Higher Education, Odisha.

References

1 Z. Qin, *Nanomaterials*, 2023, **13**, 1980.
2 S. Goswami, H. Noh, L. R. Redfern, K.-i. Otake, C.-W. Kung, Y. Cui, K. W. Chapman, O. K. Farha and J. T. Hupp, *Chem. Mater.*, 2019, **31**, 1485–1490.
3 L. Liu and A. Corma, *Chem. Rev.*, 2018, **118**, 4981–5079.
4 A. Acharya, T. B. Mete, N. Kumari, Y. Yoon, H. Jeong, T. Jang, B. Song, H. C. Choi, J. W. Han, Y. Pang, Y. Yun, A. Kumar and I. S. Lee, *Nat. Commun.*, 2023, **14**, 7667.
5 A. Kumar and L. Kumar, *Res. Chem. Intermed.*, 2024, **50**, 195–217.
6 P. Sahu, J. Shimpi and B. Prasad, in *Molecular Materials*, CRC Press, 2017, pp. 189–212.
7 R. Javed, M. Zia, S. Naz, S. O. Aisida, N. u. Ain and Q. Ao, *J. Nanobiotechnol.*, 2020, **18**, 172.
8 Q. Yu, J. Pan, J. Li, C. Su, Y. Huang, S. Bi, J. Jiang and N. Chen, *J. Mater. Chem. C*, 2022, **10**, 13143–13156.
9 E. Eom, M. Song, J.-C. Kim, D.-i. Kwon, D. N. Rainer, K. Gołąbek, S. C. Nam, R. Ryoo, M. Mazur and C. Jo, *JACS Au*, 2022, **2**, 2327–2338.
10 A. M. Jauhar, Z. Ma, M. Xiao, G. Jiang, S. Sy, S. Li, A. Yu and Z. Chen, *J. Power Sources*, 2020, **473**, 228607.
11 V. F. Yusuf, N. I. Malek and S. K. Kailasa, *ACS Omega*, 2022, **7**, 44507–44531.
12 A. E. Baumann, D. A. Burns, B. Liu and V. S. Thoi, *Commun. Chem.*, 2019, **2**, 86.
13 S. M. Moosavi, A. Nandy, K. M. Jablonka, D. Ongari, J. P. Janet, P. G. Boyd, Y. Lee, B. Smit and H. J. Kulik, *Nat. Commun.*, 2020, **11**, 4068.
14 H. Furukawa, K. E. Cordova, M. O'Keeffe and O. M. Yaghi, *Science*, 2013, **341**, 1230444.
15 D. Li, A. Yadav, H. Zhou, K. Roy, P. Thanasekaran and C. Lee, *Glob. Chall.*, 2024, **8**, 2300244.
16 I. Abánades Lázaro, X. Chen, M. Ding, A. Eskandari, D. Fairen-Jimenez, M. Giménez-Marqués, R. Gref, W. Lin, T. Luo and R. S. Forgan, *Nat. Rev. Methods Primers*, 2024, **4**, 42.
17 A. M. Wright, M. T. Kapelewski, S. Marx, O. K. Farha and W. Morris, *Nat. Mater.*, 2025, **24**, 178–187.
18 Y. Qian and H.-L. Jiang, *Acc. Chem. Res.*, 2024, **57**, 1214–1226.
19 Y. Sakamaki, M. Tsuji, Z. Heidrick, O. Watson, J. Durchman, C. Salmon, S. R. Burgin and H. Beyzavi, *J. Chem. Educ.*, 2020, **97**, 1109–1116.
20 S. Bommakanti, A. Puthukkudi, M. Samal, P. Sahu and B. P. Biswal, *Cryst. Growth Des.*, 2023, **23**, 6172–6200.
21 P. Sahu, S. Palei and U. Manju, in *Electrochemical Applications of Metal-Organic Frameworks*, ed. S. Dave, R. Sahu and B. C. Tripathy, Elsevier, 2022, pp. 95–116, DOI: 10.1016/B978-0-323-90784-2.00003-4.
22 P. Z. Moghadam, Y. G. Chung and R. Q. Snurr, *Nat. Energy*, 2024, **9**, 121–133.
23 F. Zheng, S. Cao, Z. Yang, Y. Sun, Z. Shen, Y. Wang and H. Pang, *Energy Fuels*, 2024, **38**, 11494–11520.
24 G. Li, S. Zhao, Y. Zhang and Z. Tang, *Adv. Mater.*, 2018, **30**, 1800702.
25 M. Xu, C. Lai, X. Liu, B. Li, M. Zhang, F. Xu, S. Liu, L. Li, L. Qin, H. Yi and Y. Fu, *J. Mater. Chem. A*, 2021, **9**, 24148–24174.
26 M. Duan, L. Jiang, G. Zeng, D. Wang, W. Tang, J. Liang, H. Wang, D. He, Z. Liu and L. Tang, *Appl. Mater. Today*, 2020, **19**, 100564.
27 W. Xiang, Y. Zhang, H. Lin and C.-j. Liu, *Molecules*, 2017, **22**, 2103.
28 T. Zhang, T. Li, M. Gao, W. Lu, Z. Chen, W. L. Ong, A. S. W. Wong, L. Yang, S. Kawi and G. W. Ho, *Adv. Energy Mater.*, 2024, **14**, 2400388.

29 M. Chalermnon, S. R. Thomas, J. M. Chin and M. R. Reithofer, *Inorg. Chem. Front.*, 2025, **12**, 6435–6459.
30 X. L. Ma, W. X. Shi, S. Guo, Q. P. Zhao, W. Lin, T. B. Lu and Z. M. Zhang, *Adv. Mater.*, 2025, **37**, 2506133.
31 X. Yang and Q. Xu, *Trends Chem.*, 2020, **2**, 214–226.
32 F. Ke, J. Yuan, C. Zhang, S. Ye, K. Ramachandraiah and H. Pang, *Coord. Chem. Rev.*, 2024, **518**, 216116.
33 T. Zorlu, I. B. Becerril-Castro, A. Sousa-Castillo, B. Puértolas, L. V. Besteiro, Z. Wang, A. Govorov, M. A. Correa-Duarte and R. A. Alvarez-Puebla, *Adv. Funct. Mater.*, 2024, **34**, 2410352.
34 R. Abazari, N. Ghorbani, J. Shariati, R. S. Varma and J. Qian, *Inorg. Chem.*, 2024, **63**, 12667–12680.
35 S. Sanati, R. S. Varma, M. Liu and R. Abazari, *Energy Environ. Sci.*, 2025, **18**(16), 7733–7755.
36 L. Mao and J. Qian, *Small*, 2024, **20**, 2308732.
37 Y. Deng, Y. Wang, X. Xiao, B. J. Saucedo, Z. Zhu, M. Xie, X. Xu, K. Yao, Y. Zhai and Z. Zhang, *Small*, 2022, **18**, 2202928.
38 J. Q. Ye, S. Y. Xu, Q. Liang, Y. Z. Dai and M. Y. He, *Chem. – Asian J.*, 2024, **19**, e202400161.
39 G. Yuan, L. Tan, P. Wang, Y. Wang, C. Wang, H. Yan and Y.-Y. Wang, *Cryst. Growth Des.*, 2021, **22**, 893–908.
40 R. Freund, O. Zaremba, G. Arnauts, R. Ameloot, G. Skorupskii, M. Dincă, A. Bavykina, J. Gascon, A. Ejsmont and J. Goscianska, *Angew. Chem., Int. Ed.*, 2021, **60**, 23975–24001.
41 J. Hu, Z. Huang and Y. Liu, *Angew. Chem., Int. Ed.*, 2023, **62**, e202306999.
42 L. L. Zhou, Q. Guan and Y. B. Dong, *Angew. Chem.*, 2024, **136**, e202314763.
43 J. Park, H. Kim, Y. Kang, Y. Lim and J. Kim, *JACS Au*, 2024, **4**, 3727–3743.
44 K. Sun, Y. Qian and H. L. Jiang, *Angew. Chem.*, 2023, **135**, e202217565.
45 A. Dhakshinamoorthy, Z. Li, S. Yang and H. Garcia, *Chem. Soc. Rev.*, 2024, **53**, 3002–3035.
46 H. Wang, H. Wang, Z. Wang, L. Tang, G. Zeng, P. Xu, M. Chen, T. Xiong, C. Zhou and X. Li, *Chem. Soc. Rev.*, 2020, **49**, 4135–4165.
47 Z. Wang, H. Fei and Y. n. Wu, *ChemSusChem*, 2024, **17**, e202400504.
48 T. Li, P. Wang, M. He, T. Zhang, C. Yang and Z. Li, *Coord. Chem. Rev.*, 2024, **521**, 216179.
49 M. Li, H. Zhang, C. Li, F. Lang, S.-W. Yao, J. Pang and X.-H. Bu, *Precis. Chem.*, 2025, **3**, 424–450.
50 Y. An, T. Cai, W. Jiang, T. Lei and H. Pang, *Green Chem.*, 2025, **27**, 10478–10509.
51 Y. Ou, Y. Zhang, W. Luo, Y. Wu and Y. Wang, *Macromol. Rapid Commun.*, 2025, **46**, 2401149.
52 P. Asselin and P. D. Harvey, *ACS Appl. Nano Mater.*, 2022, **5**, 6055–6082.
53 H. L. Nguyen, *Sol. RRL*, 2021, **5**, 2100198.
54 Y. Yang, Z. Sun, Y. Wu, Z. Liang, F. Li, M. Zhu and J. Liu, *Small*, 2024, **20**, 2401457.
55 Q. Zhang, S. Jiang, T. Lv, Y. Peng and H. Pang, *Adv. Mater.*, 2023, **35**, 2305532.
56 T. Shaikh, S. Pise, R. Bhosale, M. Vadiyar, K.-W. Nam and S. Kolekar, *Energy Fuels*, 2025, **39**, 2396–2421.
57 L. Huang, M. Du, D. Sun, M. He, Z. Liu, R. Wu, Y. Jiang, L. Qi, J. Wang and C. Zhu, *Small*, 2024, **20**, 2306508.
58 S. A. Fatah and K. M. Omer, *ACS Appl. Mater. Interfaces*, 2025, **17**, 11578–11594.
59 S. S. Mohammed Ameen, A. Bedair, M. Hamed, F. R. Mansour and K. M. Omer, *ACS Appl. Mater. Interfaces*, 2024, **17**, 110–129.
60 P. Hazra, S. Vadnere, S. Mishra, S. Halder, S. Mandal and P. Ghosh, *ACS Appl. Mater. Interfaces*, 2023, **15**, 52065–52082.
61 A. Schlachter, P. Asselin and P. D. Harvey, *ACS Appl. Mater. Interfaces*, 2021, **13**, 26651–26672.
62 C. Yu, L. Xu, F. Zhao, L. Kong, Y. Chen, L. Li, Z. Zhu and L. Jiang, *ACS Mater. Lett.*, 2024, **6**, 5454–5478.
63 J. Li, X. Zhou, J. Wang and X. Li, *Ind. Eng. Chem. Res.*, 2019, **58**, 15394–15406.
64 C. Guo, F. Duan, S. Zhang, L. He, M. Wang, J. Chen, J. Zhang, Q. Jia, Z. Zhang and M. Du, *J. Mater. Chem. A*, 2022, **10**, 475–507.
65 C. Zhang, Y. Wu, D. Li and H.-L. Jiang, *Chem. Sci.*, 2025, **16**, 13149–13172.
66 X. C. Qi, F. Lang, C. Li, M. W. Liu, Y. F. Wang and J. Pang, *ChemPlusChem*, 2024, **89**, e202400158.
67 C. Gao, F. Lyu and Y. Yin, *Chem. Rev.*, 2020, **121**, 834–881.
68 C. Liu, W. Wang, B. Liu, J. Qiao, L. Lv, X. Gao, X. Zhang, D. Xu, W. Liu and J. Liu, *Catalysts*, 2019, **9**, 658.
69 S. Kumar, B. Z. Dholakiya and R. Jangir, *ACS Appl. Mater. Interfaces*, 2023, **16**, 1553–1563.
70 G. Ye, G. Shi, R. Huang, X. Liu, J. Zhou, S. Wen and Q. Zhang, *Inorg. Chem.*, 2025, **64**(15), 7806–7817.
71 S. E. Alavi, S. F. Alavi, M. Koohi, A. Raza and H. Ebrahimi Shahmabadi, *J. Pharm. Invest.*, 2024, **54**, 751–783.
72 L. Li, H. Zhao, J. Wang and R. Wang, *ACS Nano*, 2014, **8**, 5352–5364.
73 M. Bhadra, H. S. Sasmal, A. Basu, S. P. Midya, S. Kandambeth, P. Pachfule, E. Balaraman and R. Banerjee, *ACS Appl. Mater. Interfaces*, 2017, **9**, 13785–13792.
74 S. B. Kalidindi, H. Oh, M. Hirscher, D. Esken, C. Wiktor, S. Turner, G. Van Tendeloo and R. A. Fischer, *Chem. – Eur. J.*, 2012, **18**, 10848–10856.
75 Y. Chen, Q. Zhou and J. Zheng, *ACS Sustainable Chem. Eng.*, 2022, **10**, 1961–1971.
76 F. Pan, C. Tong, N. Wang, Y. Wang, D. Pan and R. Zhu, *ACS Sustainable Chem. Eng.*, 2022, **10**, 16027–16036.
77 T. Pan, I. E. Khalil, Z. Xu, H. Li, X. Zhang, G. Xiao, W. Zhang, Y. Shen and F. Huo, *Nano Res.*, 2022, **15**, 1178–1182.
78 H.-L. Jiang, T. Akita, T. Ishida, M. Haruta and Q. Xu, *J. Am. Chem. Soc.*, 2011, **133**, 1304–1306.
79 Y.-Z. Chen, Q. Xu, S.-H. Yu and H.-L. Jiang, *Small*, 2015, **11**, 71–76.
80 X. Xie, X. Zhang, M. Xie, L. Xiong, H. Sun, Y. Lu, Q. Mu, M. H. Rummeli, J. Xu, S. Li, J. Zhong, Z. Deng, B. Ma, T. Cheng, W. A. Goddard and Y. Peng, *Nat. Commun.*, 2022, **13**, 63.
81 J. Hermannsdörfer, M. Friedrich, N. Miyajima, R. Q. Albuquerque, S. Kümmel and R. Kempe, *Angew. Chem., Int. Ed.*, 2012, **51**, 11473–11477.

82 F. Chen, K. Shen, J. Chen, X. Yang, J. Cui and Y. Li, *ACS Cent. Sci.*, 2019, **5**, 176–185.
83 X.-J. Bai, X. Zhai, L.-Y. Zhang, Y. Fu and W. Qi, *Matter*, 2021, **4**, 2919–2935.
84 A. Aijaz, A. Karkamkar, Y. J. Choi, N. Tsumori, E. Rönnebro, T. Autrey, H. Shioyama and Q. Xu, *J. Am. Chem. Soc.*, 2012, **134**, 13926–13929.
85 Q.-L. Zhu, J. Li and Q. Xu, *J. Am. Chem. Soc.*, 2013, **135**, 10210–10213.
86 Y.-Z. Chen, Y.-X. Zhou, H. Wang, J. Lu, T. Uchida, Q. Xu, S.-H. Yu and H.-L. Jiang, *ACS Catal.*, 2015, **5**, 2062–2069.
87 R. Tao, K. Kang, X. Li, R. Li, R. Huang, Y. Jin, L. Qiu and W. Zhang, *Inorg. Chem.*, 2021, **60**, 12517–12525.
88 M. Guo, Q. Meng, W. Chen, Z. Meng, M. L. Gao, Q. Li, X. Duan and H. L. Jiang, *Angew. Chem., Int. Ed.*, 2023, **62**, e202305212.
89 X. Lan, C. Du, L. Cao, T. She, Y. Li and G. Bai, *ACS Appl. Mater. Interfaces*, 2018, **10**, 38953–38962.
90 S. Lu, Y. Hu, S. Wan, R. McCaffrey, Y. Jin, H. Gu and W. Zhang, *J. Am. Chem. Soc.*, 2017, **139**, 17082–17088.
91 B. Mishra, S. Biswal and B. P. Tripathi, *ACS Appl. Nano Mater.*, 2024, **7**, 5317–5328.
92 L. Chen, H. Chen, R. Luque and Y. Li, *Chem. Sci.*, 2014, **5**, 3708–3714.
93 B. An, J. Zhang, K. Cheng, P. Ji, C. Wang and W. Lin, *J. Am. Chem. Soc.*, 2017, **139**, 3834–3840.
94 R.-D. Ding, Y.-L. Li, F. Leng, M.-J. Jia, J.-H. Yu, X.-F. Hao and J.-Q. Xu, *ACS Appl. Nano Mater.*, 2021, **4**, 9790–9798.
95 L. Chen, B. Huang, X. Qiu, X. Wang, R. Luque and Y. Li, *Chem. Sci.*, 2016, **7**, 228–233.
96 W. Qin, W. Cao, H. Liu, Z. Li and Y. Li, *RSC Adv.*, 2014, **4**, 2414–2420.
97 Y. Yang, H. Noh, Q. Ma, R. Wang, Z. Chen, N. M. Schweitzer, J. Liu, K. W. Chapman and J. T. Hupp, *ACS Appl. Mater. Interfaces*, 2021, **13**, 36232–36239.
98 W.-G. Cui, Y.-T. Li, H. Zhang, Z.-C. Wei, B.-H. Gao, J.-J. Dai and T.-L. Hu, *Appl. Catal., A*, 2020, **278**, 119262.
99 Y. Shen, L.-W. Bao, F.-Z. Sun and T.-L. Hu, *Mater. Chem. Front.*, 2019, **3**, 2363–2373.
100 L. Wang, K. Zhang, J. Li, X. Shen, N. Yan, H.-Z. Zhao and Z. Qu, *Environ. Sci. Technol.*, 2022, **56**, 16240–16248.
101 Y. Fang, Z. Xiao, J. Li, C. Lollar, L. Liu, X. Lian, S. Yuan, S. Banerjee, P. Zhang and H.-C. Zhou, *Angew. Chem., Int. Ed.*, 2018, **57**, 5283–5287.
102 M. Zhong, S. Zhang, A. Dong, Z. Sui, L. Feng and Q. Chen, *J. Mater. Sci.*, 2020, **55**, 10388–10398.
103 L. Chen, X. Chen, H. Liu, C. Bai and Y. Li, *J. Mater. Chem. A*, 2015, **3**, 15259–15264.
104 M. S. El-Shall, V. Abdelsayed, A. E. R. S. Khder, H. M. A. Hassan, H. M. El-Kaderi and T. E. Reich, *J. Mater. Chem.*, 2009, **19**, 7625–7631.
105 H. Duan, Y. Zeng, X. Yao, P. Xing, J. Liu and Y. Zhao, *Chem. Mater.*, 2017, **29**, 3671–3677.
106 B. Zhang, Y. Pei, R. V. Maligal-Ganesh, X. Li, A. Cruz, R. J. Spurling, M. Chen, J. Yu, X. Wu and W. Huang, *Ind. Eng. Chem. Res.*, 2020, **59**, 17495–17501.
107 M. Zhang, Q. Shang, Y. Wan, Q. Cheng, G. Liao and Z. Pan, *Appl. Catal., B*, 2019, **241**, 149–158.
108 L. Zhou, Y. An, J. Ma, G. Hao, Z. Li, J. Chen and L.-Y. Chou, *Chem. Sci.*, 2023, **14**, 13126–13133.
109 Q. Yang, W. Liu, B. Wang, W. Zhang, X. Zeng, C. Zhang, Y. Qin, X. Sun, T. Wu, J. Liu, F. Huo and J. Lu, *Nat. Commun.*, 2017, **8**, 14429.
110 Q. Yang, W. Liu, B. Wang, W. Zhang, X. Zeng, C. Zhang, Y. Qin, X. Sun, T. Wu and J. Liu, *Nat. Commun.*, 2017, **8**, 14429.
111 L. Chen, W. Wang, J. Tian, F. Bu, T. Zhao, M. Liu, R. Lin, F. Zhang, M. Lee, D. Zhao and X. Li, *Nat. Commun.*, 2021, **12**, 4556.
112 L.-N. Chen, H.-Q. Li, M.-W. Yan, C.-F. Yuan, W.-W. Zhan, Y.-Q. Jiang, Z.-X. Xie, Q. Kuang and L.-S. Zheng, *Small*, 2017, **13**, 1700683.
113 B. Wang, W. Liu, W. Zhang and J. Liu, *Nano Res.*, 2017, **10**, 3826–3835.
114 J. W. M. Osterrieth, D. Wright, H. Noh, C.-W. Kung, D. Vulpe, A. Li, J. E. Park, R. P. Van Duyne, P. Z. Moghadam, J. J. Baumberg, O. K. Farha and D. Fairen-Jimenez, *J. Am. Chem. Soc.*, 2019, **141**, 3893–3900.
115 H. Robatjazi, D. Weinberg, D. F. Swearer, C. Jacobson, M. Zhang, S. Tian, L. Zhou, P. Nordlander and N. J. Halas, *Sci. Adv.*, 2019, **5**, eaav5340.
116 K. Nakatsuka, T. Yoshii, Y. Kuwahara, K. Mori and H. Yamashita, *Chem. – Eur. J.*, 2018, **24**, 898–905.
117 Z. Li, R. Yu, J. Huang, Y. Shi, D. Zhang, X. Zhong, D. Wang, Y. Wu and Y. Li, *Nat. Commun.*, 2015, **6**, 8248.
118 J. Wang, H. Xu, C. Ao, X. Pan, X. Luo, S. Wei, Z. Li, L. Zhang, Z.-l. Xu and Y. Li, *iScience*, 2020, **23**, 101233.
119 Y. Su, H. Xu, J. Wang, X. Luo, Z.-l. Xu, K. Wang and W. Wang, *Nano Res.*, 2019, **12**, 625–630.
120 T. Inomata and K. Konishi, *Chem. Commun.*, 2003, (11), 1282–1283.
121 Y. Long, S. Song, J. Li, L. Wu, Q. Wang, Y. Liu, R. Jin and H. Zhang, *ACS Catal.*, 2018, **8**, 8506–8512.
122 M. Shi, D. Luo, R. Liu, J. Wei, S. Guo, Z. Lu and Y. Ni, *Inorg. Chem.*, 2024, **63**, 18233–18241.
123 H. He, L. Li, Y. Liu, M. Kassymova, D. Li, L. Zhang and H.-L. Jiang, *Nano Res.*, 2021, **14**, 444–449.
124 L. Chen, H. Chen and Y. Li, *Chem. Commun.*, 2014, **50**, 14752–14755.
125 K. Wang, W. Zhao, Q. Zhang, H. Li and F. Zhang, *ACS Omega*, 2020, **5**, 16183–16188.
126 H. Gamraoui, A. Khojastehnezhad, M. Bélanger-Bouliga, A. Nazemi and M. Siaj, *ACS Appl. Nano Mater.*, 2024, **7**, 22570–22580.
127 L. Chen, X. Chen, H. Liu and Y. Li, *Small*, 2015, **11**, 2642–2648.
128 Y. Liu, C.-H. Liu, T. Debnath, Y. Wang, D. Pohl, L. V. Besteiro, D. M. Meira, S. Huang, F. Yang, B. Rellinghaus, M. Chaker, D. F. Perepichka and D. Ma, *Nat. Commun.*, 2023, **14**, 541.
129 Y. Jiang, X. Zhang, X. Dai, W. Zhang, Q. Sheng, H. Zhuo, Y. Xiao and H. Wang, *Nano Res.*, 2017, **10**, 876–889.
130 H. Alamgholiloo, S. Rostamnia, A. Hassankhani, X. Liu, A. Eftekhari, A. Hasanzadeh, K. Zhang, H. Karimi-Maleh, S.

Khaksar and R. S. Varma, *J. Colloid Interface Sci.*, 2020, **567**, 126–135.
131 S. Muhamed, R. K. Aparna, A. Karmakar, S. Kundu and S. Mandal, *Nanoscale*, 2022, **14**, 17345–17353.
132 H. Issa Hamoud, P. Damacet, D. Fan, N. Assaad, O. I. Lebedev, A. Krystianiak, A. Gouda, O. Heintz, M. Daturi and G. Maurin, *J. Am. Chem. Soc.*, 2022, **144**, 16433–16446.
133 H. Wang, X. Liu, Y. Zhao, Z. Sun, Y. Lin, T. Yao and H.-L. Jiang, *Natl. Sci. Rev.*, 2024, **11**, nwae252.
134 N. Tsumori, L. Chen, Q. Wang, Q.-L. Zhu, M. Kitta and Q. Xu, *Chem*, 2018, **4**, 845–856.
135 F. Yang, W. Hu, C. Yang, M. Patrick, A. L. Cooksy, J. Zhang, J. A. Aguiar, C. Fang, Y. Zhou, Y. S. Meng, J. Huang and J. Gu, *Angew. Chem., Int. Ed.*, 2020, **59**, 4572–4580.
136 C. Wang, K. E. deKrafft and W. Lin, *J. Am. Chem. Soc.*, 2012, **134**, 7211–7214.
137 M. R. Mian, L. R. Redfern, S. M. Pratik, D. Ray, J. Liu, K. B. Idrees, T. Islamoglu, L. Gagliardi and O. K. Farha, *Chem. Mater.*, 2020, **32**, 3078–3086.
138 C. Zhan, M. Moskovits and Z.-Q. Tian, *Matter*, 2020, **3**, 42–56.
139 S. Ezendam, M. Herran, L. Nan, C. Gruber, Y. Kang, F. Gröbmeyer, R. Lin, J. Gargiulo, A. Sousa-Castillo and E. Cortés, *ACS Energy Lett.*, 2022, **7**, 778–815.
140 C. S. L. Koh, H. Y. F. Sim, S. X. Leong, S. K. Boong, C. Chong and X. Y. Ling, *ACS Mater. Lett.*, 2021, **3**, 557–573.
141 A. Amirjani, N. B. Amlashi and Z. S. Ahmadiani, *ACS Appl. Nano Mater.*, 2023, **6**, 9085–9123.
142 Y. Qin, M. Hao, J. Wang, R. Yuan and Z. Li, *ACS Appl. Mater. Interfaces*, 2022, **14**, 56930–56937.
143 M. Wen, K. Mori, Y. Kuwahara and H. Yamashita, *ACS Energy Lett.*, 2017, **2**, 1–7.
144 Y. Shen, T. Pan, P. Wu, J. Huang, H. Li, I. E. Khalil, S. Li, B. Zheng, J. Wu, Q. Wang, W. Zhang, W. D. Wei and F. Huo, *CCS Chem.*, 2021, **3**, 1607–1614.
145 J.-D. Xiao, Q. Shang, Y. Xiong, Q. Zhang, Y. Luo, S.-H. Yu and H.-L. Jiang, *Angew. Chem., Int. Ed.*, 2016, **55**, 9389–9393.
146 W. Zhen, H. Gao, B. Tian, J. Ma and G. Lu, *ACS Appl. Mater. Interfaces*, 2016, **8**, 10808–10819.
147 Y. Liu, Y. Shi, H. Wang and S. Zhang, *Nano Res.*, 2024, **17**, 5835–5844.
148 F. Kong and W. Chen, *Nanomaterials*, 2024, **14**, 1340.
149 S. Fu, S. Yao, S. Guo, G.-C. Guo, W. Yuan, T.-B. Lu and Z.-M. Zhang, *J. Am. Chem. Soc.*, 2021, **143**, 20792–20801.
150 S. Nitopi, E. Bertheussen, S. B. Scott, X. Liu, A. K. Engstfeld, S. Horch, B. Seger, I. E. L. Stephens, K. Chan, C. Hahn, J. K. Nørskov, T. F. Jaramillo and I. Chorkendorff, *Chem. Rev.*, 2019, **119**, 7610–7672.
151 T. Kawawaki, T. Okada, K. Takemae, S. Tomihari and Y. Negishi, *ChemNanoMat*, 2024, **10**, e202300575.
152 Q.-J. Wu, D.-H. Si, P.-P. Sun, Y.-L. Dong, S. Zheng, Q. Chen, S.-H. Ye, D. Sun, R. Cao and Y.-B. Huang, *Angew. Chem., Int. Ed.*, 2023, **62**, e202306822.
153 M. Zhang, M. Lu, M.-Y. Yang, J.-P. Liao, Y.-F. Liu, H.-J. Yan, J.-N. Chang, T.-Y. Yu, S.-L. Li and Y.-Q. Lan, *eScience*, 2023, **3**, 100116.
154 C.-W. Kung, C. O. Audu, A. W. Peters, H. Noh, O. K. Farha and J. T. Hupp, *ACS Energy Lett.*, 2017, **2**, 2394–2401.
155 M. Chen, L. Han, J. Zhou, C. Sun, C. Hu, X. Wang and Z. Su, *Nanotechnology*, 2018, **29**, 284003.
156 K. M. Choi, D. Kim, B. Rungtaweevoranit, C. A. Trickett, J. T. D. Barmanbek, A. S. Alshammari, P. Yang and O. M. Yaghi, *J. Am. Chem. Soc.*, 2017, **139**, 356–362.
157 Y. Han, H. Xu, Y. Su, Z.-l. Xu, K. Wang and W. Wang, *J. Catal.*, 2019, **370**, 70–78.
158 S. Yao, S. Y. Jiang, B. F. Wang, H. Q. Yin, X. Y. Xiang, Z. Tang, C. H. An, T. B. Lu and Z. M. Zhang, *Am. Ethnol.*, 2025, **137**, e202418637.
159 C.-P. Wan, H. Guo, D.-H. Si, S.-Y. Gao, R. Cao and Y.-B. Huang, *JACS Au*, 2024, **4**, 2514–2522.
160 Z. Yang, A. Li, H. Li, G. Lai, Y. Fu, Y. Zhang, K. Wang, S. Zeng, L. Xie and M. Li, *Angew. Chem., Int. Ed.*, 2025, **64**(19), e202505399.
161 X. Chu, S. Liu, B. B. Luan, Y. Zhang, Y. Xi, L. H. Shao, F. M. Zhang and Y. Q. Lan, *Am. Ethnol.*, 2025, **137**, e202422940.
162 W. Han, M. Shi and H. L. Jiang, *Angew. Chem., Int. Ed.*, 2025, **64**, e202421942.
163 Y. Q. Zhang, M. Liu, L. T. Zhang, N. Lu, X. Wang, Z. G. Li, X. H. Zhang, N. Li and X. H. Bu, *Adv. Funct. Mater.*, 2025, **35**, 2412406.
164 Y. Fei, R. Abazari, M. Ren, X. Wang and X. Zhang, *Inorg. Chem.*, 2024, **63**, 18914–18923.